

A neural network-based four-body potential energy surface for parahydrogen

Alexander Ibrahim^{1,2} and Pierre-Nicholas Roy^{2, a)}

¹⁾Department of Physics and Astronomy, University of Waterloo, 200 University Avenue West, Waterloo, Ontario N2L 3G1, Canada

²⁾Department of Chemistry, University of Waterloo, 200 University Avenue West, Waterloo, Ontario N2L 3G1, Canada

We present an isotropic *ab initio* (*para*-H₂)₄ four-body interaction potential energy surface (PES). The electronic structure calculations are performed at the correlated coupled-cluster theory level, with single, double, and perturbative triple excitations. They use an atom-centred augmented correlation-consistent double zeta basis set, supplemented by a (3s3p2d) midbond function. We use a multilayer perceptron to construct the PES. We apply a rescaling transformation to the output energies during training to improve the prediction of weaker energies in the sample data. At long distances, the interaction energies are adjusted to match the empirically-derived four-body dispersion interaction. The four-body interaction energy at short intermolecular separations is net repulsive. The use of this four-body PES, in combination with a first principles pair potential for *para*-H₂ [J. Chem. Phys. **119**, 12551 (2015)], and an isotropic *ab initio* three-body potential for *para*-H₂ [J. Chem. Phys. **156**, 044301 (2022)], is expected to provide closer agreement with experimental results.

I. INTRODUCTION

The topic of many-body intermolecular interactions has seen a rise in interest over the past few decades.^{1–6} Hydrogen, as the simplest molecular species, is an excellent subject for the study of many-body interactions. One of its nuclear spin isomers, parahydrogen (*para*-H₂) displays a variety of exotic quantum behaviors in many-body systems. For example, solid *para*-H₂ is a quantum molecular solid.^{7–11} The individual *para*-H₂ molecules that comprise it have relatively large zero-point energies.^{8,11–13} This gives each molecule very large amplitude vibrations about its nominal lattice site, which “inflates” the lattice and gives the solid a much larger molar volume than one would expect from a classical description.^{13,14}

It has become increasingly apparent that condensed many-body systems of *para*-H₂ molecules, especially at high densities, cannot be adequately modelled using only pairwise additive interactions.^{15–18} This appears strange at first, because three-body and higher-order many-body interactions are strong only at very short ranges.¹⁹ However, these many-body interactions contribute significantly at much lower densities than one would expect classically, mainly because each *para*-H₂ molecule has such a delocalized probability distribution.

Introducing many-body interactions into these models is a challenging task. Pair interactions can often be reduced to a one-dimensional function of distance. However, interactions between three or more particles require several parameters to properly describe, and are necessarily multi-dimensional.⁵ Recent developments in multiple research fronts have made it possible to create potential energy surfaces (PES) for many-body systems. Advances in computational chemistry together

with increased computing power make it possible to perform *ab initio* electronic structure calculations for large collections of particles. Also, the widespread availability of machine learning software makes it much easier to create higher dimensional PESs for many-body interactions.^{20,21}

Consider a collection of N *para*-H₂ molecules. Let the coordinate \mathbf{R}_i describe the position and angular orientation of the i^{th} particle. The total interaction potential energy of the system V_{tot} can be expanded as a sum of many-body potentials using

$$V_{\text{tot}} = \sum_{i < j}^N V_2(\mathbf{R}_i, \mathbf{R}_j) + \sum_{i < j < k}^N V_3(\mathbf{R}_i, \mathbf{R}_j, \mathbf{R}_k) + \sum_{i < j < k < l}^N V_4(\mathbf{R}_i, \mathbf{R}_j, \mathbf{R}_k, \mathbf{R}_l) + \dots \quad (1)$$

where V_2 is the two-body interaction potential, V_3 is the three-body interaction potential, and so on.

Most research on interaction potentials between hydrogen molecules focuses on the pair potential. With hydrogen being the simplest molecule, there is no shortage of examples of two-body interaction potentials.^{22–31} Pair potentials for hydrogen molecules have several common features. They have a repulsive wall at short intermolecular distances, a somewhat deep attractive well (typically centred around 3.0 Å), and a weakly decaying attractive tail for the dispersion interaction. A common issue with several H₂ and *para*-H₂ pair potentials is that the repulsive wall is too strong. This leads to a severe overestimation of the pressure when modelling condensed systems of *para*-H₂ at high densities.^{32,33} At short intermolecular separations, pair potentials on their own become unreliable, and we require many-body interactions to accurately describe collections of *para*-H₂ molecules.^{16–18}

It is well known that the next order interaction, the three-body interaction potential for *para*-H₂, is overall attractive at short intermolecular distances.^{16–19} One

^{a)}Electronic mail: pnroy@uwaterloo.ca

common three-body analytic potential is the Axilrod-Teller-Muto (ATM) potential.^{34,35} It accurately models the dispersion relation at large distances, but incorrectly predicts the short-range interaction to be net repulsive. In 2010, Manzhos *et al.* published a machine-learning based three-body PES for *para*-H₂.¹⁸ Recently, our group published an isotropic 3D *ab initio* three-body PES for *para*-H₂.¹⁹ Its energies are calculated at the correlated coupled-cluster theory level, with single, double, and perturbative triple excitations (CCSD(T)). The calculations use an atom-centred augmented correlation-consistent triple zeta (AVTZ) basis set, supplemented by a (3s3p2d) midbond function.³⁶ We use the reproducing-kernel Hilbert Space method to fit the energies.³⁷⁻⁴⁰

Recently, we performed simulations of solid *para*-H₂ using the two-body Faruk-Schmidt-Hinde (FSH) potential³¹ and our recent three-body PES.⁴¹ Due to its repulsive character at short distances, simulations that use only the FSH potential overestimate the pressure-density equation of state (EOS) at high densities.⁴² Because the three-body PES is net attractive, its inclusion alongside the pair PES decreases the pressure. At low densities, this change slightly improves the agreement of the simulations with experiment. However, at high densities, the three-body PES overcorrects the repulsive effects of the pair PES, and greatly underestimates the pressure.

Wheatley *et al.* recently published an *ab initio* four-body PES for helium.⁴³ The energies were calculated at the CCSD(T) level, using an AVQZ atom-centred basis set. The interpolation for the PES is based on Gaussian processes.⁴⁴ They performed path-integral Monte Carlo (PIMC) simulations using this potential to calculate the fourth virial coefficient of helium to reasonable agreement with experiment over a wide range of temperatures. The four-body PES for helium shares many qualitative features with the four-body PES for *para*-H₂ presented in this paper.

In this paper, we present a six-dimensional, isotropic four-body PES for *para*-H₂. The energies are calculated at the CCSD(T) level of theory, using an AVDZ atom-centred basis set, with an additional (3s3p2d) midbond function at the centre of mass of each calculation.³⁶ We use a rigid rotor approximation and average out the rotational degrees of freedom using the 6-point Lebedev quadrature⁴⁵ to make the interactions isotropic. We model the PES using a multi-layer perceptron, trained using PyTorch.²⁰ At large intermolecular separations, we use an analytic four-body interaction potential to more accurately describe the dispersion interaction.^{46,47} At short range, we fit the energies to an exponential decay, with some modifications for numerical stability.

The remainder of this paper is structured as follows: Sec. (II) goes over the creation of the PES, including the calculation of the interaction energies and how the degrees of freedom are managed. It also covers how the training data is generated, the transformations on the inputs and outputs that improve the effectiveness of the training, and the training process itself. Sec. (III) is a

discussion and analysis of the PES. It includes an error analysis of the electronic structure calculations and the methods used to manage the degrees of freedom. It also covers the short-range and long-range extrapolations of the PES, and ends with an analysis of the effects of the four-body interaction on a classical approximation of solid *para*-H₂.

II. CREATING THE POTENTIAL ENERGY SURFACE

A. Electronic Structure Calculations

We use the MRCC software program (version 2019)⁴⁸ to carry out the electronic structure calculations for the (H₂)₄ energies. The calculations are performed at the CCSD(T) level of theory.⁴⁹ There is an AVDZ basis set centred at each of the eight hydrogen atoms. We supplement the basis with (3s3p2d) midbond functions³⁶ located at the centre of mass of the collection of atoms, as was done for the pair potential by Hinde²⁹ and this group's recent three-body PES.¹⁹ An analysis of different basis sets and electronic structure methods is given in Sec. (III B).

There are many settings available in the MRCC program that determine the precision of the energy calculations. All calculations provided in this paper were carried out using the default settings, except for `cctol`, which is set to 9, and `scftol` and `scfdtol`, which are both set to 7. Under these settings, the final iterations in the SCF and CCSD calculations change on the order of 10⁻¹¹ Hartrees and 10⁻¹⁰ Hartrees, respectively. Nearly all SCF and CCSD energy calculations converged within 9 and 20 iterations, respectively. After the conversion to wavenumbers and the sum of terms needed to find the interaction energy, we estimate a conservative upper bound of 10⁻⁴ cm⁻¹ on the convergence error of the interaction energies. As a test, we select a handful of calculations for the tetrahedron geometry (as presented in Sec. (III B)), with side lengths ranging from 2.2 Å to 4.5 Å. We perform them once more, but with the value of `cctol` set to 10 instead of 9. Of the differences between the energies in our samples when `cctol=10` and `cctol=9`, the mean absolute difference was 7.2 × 10⁻⁶ cm⁻¹, whereas the maximum absolute difference was 2.7 × 10⁻⁵ cm⁻¹.

Let $\mathbf{R}_i = (\mathbf{r}_i, \rho_i, \Omega_i)$ describe the centre-of-mass position, bond length, and space-fixed angular orientation of the *i*th hydrogen molecule, respectively. Let $E_{ijkl} = E_{ijkl}(\mathbf{R}_i, \mathbf{R}_j, \mathbf{R}_k, \mathbf{R}_l)$ be the CCSD(T) energy with all molecules *i*, *j*, *k*, and *l* present. Define E_{ijk} to be the CCSD(T) energy with only molecules *i*, *j*, and *k* present, but still in the full four-body basis set. In other words, despite the charge of molecule *l* being missing, the atom-centred basis of molecule *l* is still present. We define E_{ij} and E_i similarly, in that a missing index indicates that the molecule is missing but its basis set is still present. The counterpoise-corrected⁵⁰ interaction energy of four hydrogen molecules (with $(\mathbf{R}_i, \mathbf{R}_j, \mathbf{R}_k, \mathbf{R}_l)$ omitted for

brevity) is given by

$$\begin{aligned} \Delta E = & E_{1234} \\ & - (E_{123} + E_{124} + E_{134} + E_{234}) \\ & + (E_{12} + E_{13} + E_{14} + E_{23} + E_{24} + E_{34}) \\ & - (E_1 + E_2 + E_3 + E_4). \end{aligned} \quad (2)$$

Each interaction energy requires 15 separate electronic structure calculations to produce.

B. Managing Degrees of Freedom

By modelling the molecules as a collection of four rotors in free space, we can describe the system as having 4 degrees of freedom from the bond lengths, 8 degrees of freedom from the angular orientations of the rotors, and 6 degrees of freedom from the distances between their centres of mass, for a total of 18 degrees of freedom.

We can use the rigid rotor approximation to fix the bond length of each molecule to the vibrationally averaged ground state length of 1.449 a_0 ,¹⁷ removing four degrees of freedom.

The eight degrees of freedom associated with the angular orientations are removed by performing a 6-point Lebedev quadrature.^{45,51,52} To perform this averaging, we first fix in space the centres of mass of each of the four hydrogen molecules. Next we align each rigid H_2 molecule along either the space-fixed x -, y -, or z -axis, giving each molecule 3 possible angular orientations. This alignment is done independently for each of the four hydrogen molecules, for a total of 81 different combinations of space-fixed angular orientations. Let n label each of the 81 different combinations. Performing the energy calculation described in Eq. (2) for the n^{th} combination gives the interaction energy $\Delta E^{(n)}$. The isotropic four-body interaction energy is the average of these 81 interaction energies.

$$V_4 = \frac{1}{81} \sum_{n=1}^{81} \Delta E^{(n)}(\{\mathbf{R}_i\}). \quad (3)$$

where $\{\mathbf{R}_i\} = (\mathbf{R}_1, \mathbf{R}_2, \mathbf{R}_3, \mathbf{R}_4)$. This averaging process projects out the anisotropic components of the interaction energy. It is an approximation to performing the full integration over all the degrees of freedom. There are higher levels of Lebedev quadratures that give more accurate averages, but require many more energy calculations to perform the average.⁴⁵ In an analysis given in Sec. (III A), we show that the next highest Lebedev quadrature give a negligible improvement in the accuracy.

After removing the bond length and angular orientation degrees of freedom, we have reduced the description of our system from that of four interacting rotors to that of four interacting points in space (see Fig. 1). We are now left with only 6 degrees of freedom, corresponding to the relative distances between the centres of

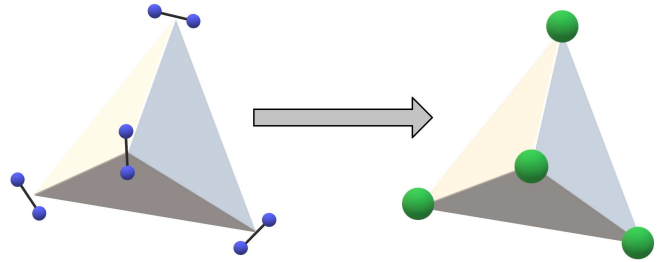


FIG. 1. A graphical representation of how fixing the bond length of each hydrogen molecule, and averaging over the angular orientations of the system, means we now model the four hydrogen molecules as four points in space.

mass of each pair of hydrogen molecules. We can thus describe each four-body geometry with the six relative side lengths $\{r_{ij}\} = (r_{12}, r_{13}, r_{14}, r_{23}, r_{24}, r_{34})$ where r_{ij} is the distance between the centres of mass of molecules i and j . For the remainder of the paper, when we refer to the “distance between two molecules,” we mean specifically the distance between each molecule’s centre of mass. Also, when we refer to the “interaction energy of a four-body geometry,” we refer to the isotropic interaction energy between four *para*- H_2 molecules, where the centres of mass of the molecules lie at the corners of the aforementioned four-body geometry.

Notice that each interaction energy is a linear combination of 15 separate CCSD(T) energies, each requiring its own electronic structure calculation. Moreover, each 6-point Lebedev quadrature is a linear combination of 81 separate interaction energies. This means that each averaged energy value requires a total of 1215 individual CCSD(T) energy values.

C. Sample Generation

To train the neural network and create the PES, we need to generate samples for training, testing, and validation. The inputs are the ordered set of six side lengths $(r_{12}, r_{13}, r_{14}, r_{23}, r_{24}, r_{34})$ and the outputs are the corresponding four-body interaction energy as given by Eq. (3). This PES is meant to be used in numerical simulations, including at high densities, and thus interaction energies at short distances must be well represented in the training data. At longer intermolecular separations, the *ab initio* CCSD(T) energies converge to the four-body dispersion relation (see Sec. (III B)).^{46,47} Thus we do not have to sample energies from geometries with excessively large intermolecular separations, even for purposes where the weak long-range energies are important, such as simulations involving the gas phase.⁵³

The procedure for generating samples is as follows. First, we decide on an exponential decay sampling function

$$p(r) = Q \exp\{-Cr\}, \quad (4)$$

where C is a positive constant and Q is a constant chosen to normalize the distribution between r_{\min} and r_{\max} (mentioned later). To create an input data sample, we first sample 6 side lengths *i.i.d.* from $p(r)$ between r_{\min} and r_{\max} , and label them $(r_{12}, r_{13}, r_{14}, r_{23}, r_{24}, r_{34})$. We next attempt to construct a four-body geometry from the six side lengths via trilateration.⁵⁴ However, not every ordered set of 6 side lengths can be turned into a valid 3D shape. If the 6 side lengths form a valid four-body geometry, we accept the sample. If not, we generate an entirely new ordered set of 6 side lengths, and repeat the process of attempting to construct a valid 3D shape from the side lengths until it succeeds. In the supplementary material, we provide an example of the function we use to generate the four points from the six side lengths.

There are several reasons for settling upon this sampling strategy. First, it allows us to generate samples with different, uncorrelated side lengths, which is important because we do not know *a priori* the probability distribution of the *para*-H₂ molecules in the situation the PES is used in. Second, an exponential decay function allows us to generate samples to have shorter side lengths with a greater frequency than longer side lengths. This is desirable, because samples with excessively long pair distances have energies that are either negligibly weak or can be replaced with the analytic four-body dispersion interaction described in Sec. (III D). By choosing the value of C , we can determine the distribution of side lengths, and therefore roughly determine the energies. For example, a large value of C causes Eq. (4) to generate smaller side lengths, which correspond to samples with larger energies. Looking at Fig. 2, it appears that we were successful in generating samples with a large range of energies, with a slight bias towards high-energy samples.

With $C_0 = 0.9209 \text{ \AA}^{-1}$, we sample 9000 points between 2.2 Å and 4.5 Å using $C = C_0$ (for a wide range of side lengths and energies), 1500 points between 2.2 Å and 4.5 Å using $C = 3C_0$ (for samples with short side lengths and large energies), 1500 points between 2.2 Å and 4.5 Å using $C = 6C_0$ (for samples with very short side lengths and very large energies), and 4000 points between 2.8 Å and 4.5 Å using $C = C_0/6$ (for samples with long side lengths and weak energies).

We supplement the training data using samples that are based specifically on the geometries of the *hcp* lattice. To generate these samples, we first select a reference molecule in the lattice. Then we consider all four-body geometries involving this reference molecule that satisfy two conditions; they have at least one side length equal to the lattice constant, and they have no side length that is more than twice the lattice constant. Geometries that disobey these conditions have a nearly negligible contribution to the total interaction energy, even at a lattice constant as low as 2.2 Å. There are 83 different four-body shapes that satisfy these conditions. For each shape, we calculate the interaction energy for 47 different lattice constants, evenly spaced between 2.2 Å and 4.5 Å, for a total of 3901 additional samples. A rescaling strategy

for training described in Sec. (II E) requires us to discard many of these *hcp* lattice-based samples, resulting in only 1610 of them being included in the training data.

The aforementioned sampling strategy for geometries has certain limitations. The range of side lengths is relatively constrained to limit the sampling of geometries with especially weak energies. This means that, within any given sample, the largest side length is at most about twice the length of any other side length. This leads to relatively “compact” geometries. Certain types of geometries, such as planar or linear geometries, are poorly represented, and if they appear at all, it is due to their presence in the *hcp* lattice-based samples.

D. Feature Transformations

For our neural network, the input data is the ordered set of six side lengths,

$$(r_{12}, r_{13}, r_{14}, r_{23}, r_{24}, r_{34}), \quad (5)$$

and the output is the corresponding interaction energy,

$$V_4 = V_4(r_{12}, r_{13}, r_{14}, r_{23}, r_{24}, r_{34}). \quad (6)$$

To simplify training and improve the performance of our model, we apply three transformations to the six side lengths. First, we take the reciprocals of each of the six side lengths. Shorter pair distances generally correspond to greater energies, and taking the reciprocal of the distance turns smaller distances into larger input features. Next we linearly map all the features onto (0, 1]. We then perform a permutation of the six features in a way that preserves the symmetry of the four-body system.

Because the four *para*-H₂ molecules are identical, our model must be invariant to the permutation of the molecule indices. However, swapping indices changes the order of the six side lengths. If, for example, we swap particle indices 1 and 2 for the six side lengths in Eq. (5), the input becomes $(r_{12}, r_{23}, r_{24}, r_{13}, r_{14}, r_{34})$. The neural network thus interprets the permuted input as a completely different sample, and produces a different output energy. On a neural network trained on data without accounting for this permutation symmetry, an index swap can even change the output energy by tens of wavenumbers at short ranges.

Not all permutations are possible. Of the $6! = 720$ permutations of these elements, only 24 of them are allowed. For example, there is no way to swap the indices such that we only interchange the first two side lengths r_{12} and r_{13} , while leaving the other four side lengths unchanged. In particular, we cannot simply sort the six side lengths as a way of solving this permutation issue. As seen later in Table II, it is possible to have two separate four-body geometries with the same six pair distances in different, permutationally-incompatible orders. In such a case, naively sorting the pair distances would make the two samples indistinguishable. In addition, not

every six-tuple input of pair distances corresponds to a valid four-body geometry, and a naive sort could generate such six-tuples.

We decide to account for the permutation symmetry at the input transformation level by selecting the “smallest” permutation, as defined by lexicographic ordering (see the supplementary material). For readers familiar with the Python programming language, this is the kind of ordering that Python uses to compare two tuples of equal size of floating-point numbers. We have a slower, naive implementation, and a much faster lookup-based implementation.

In the slower naive implementation, we loop over all 24 allowed permutations of the input (after the first two transformations), and select the one with the lowest lexicographic order. However, under certain conditions, we can come up with a much faster implementation. In the cases where the shortest and second-shortest pair distances are unique, the permutation with the lowest lexicographic order can be uniquely determined using a lookup table. In particular, in a molecular simulation the six pair distances are floating point numbers calculated from four points in space that have been perturbed from their original positions. Thus, in this case, the six pair distances are almost always unique, and this much faster solution becomes viable.

Another considered solution was to use the permutations for data augmentation. However, as seen in Sec. (II F), we propose the possibility of using small models during the simulation for improved runtime performance. When we make the model permutation invariant, the increased error from using a smaller model is easily manageable. However, when we train using permutations for data augmentation, the error from smaller models increases considerably, because there are too few parameters to fit the permutations.

E. Rescaling the Energies

The energies in the overall data set span about five orders of magnitude. Our model must be able to predict both short-range, strong-energy samples and long-range, weak-energy samples with high accuracy. Despite being much smaller in magnitude, at lower densities, the probability distribution of solid parahydrogen is predominantly in the long-range, weak-energy region of coordinate space. The mean-squared error (MSE) loss function does not prioritize the prediction of weak-energy samples during training. Other loss functions that might work well with outputs over a large range of values, such as the relative squared error, or the mean square log error, were considered, but provided unsatisfactory results.

Instead, we can take advantage of the analytically predicted behavior of the interaction potential to transform the energies in a way that makes training more effective. We create a rescaling function for the energies. This rescaling function is the sum of an exponential decay and

an r^{-12} decay function

$$\phi(r) = A \exp\{-Br\} + Cr^{-12} \quad (7)$$

where $A = 3.1803 \times 10^6 \text{ cm}^{-1}$, $B = 4.623057 \text{ \AA}^{-1}$, $C = 4220.011 \text{ \AA}^{12} \text{ cm}^{-1}$, and r is the mean of the six side lengths of a given sample. The choice of using an exponential decay and a r^{-12} power decay was to make the rescaling function somewhat resemble the features of the true underlying *ab initio* potential (see Sec. (III D)). This makes it easier to rescale the energies into a similar range. Importantly, the rescaling function is positive for the entire coordinate space of the samples. This means we can divide the *ab initio* energies by this rescaling function to recover a rescaled energy. The neural network is trained using these rescaled energy values as outputs. To recover the predicted energy from the output of a neural network, we multiply the output of the neural network by the rescaling function Eq. (7).

Certain weak-energy samples with large intermolecular separations from the *hcp* data set end up becoming very large when rescaled, due to the r^{-12} term in the denominator. These samples have large enough side lengths that their energies will be completely overwritten by the Bade potential in the final PES anyways (see Sec. (III B)). By filtering out all samples where the mean side length is greater than 4.5 Å, we can remove the outsized influence of these samples on the loss function, and improve our rescaling strategy. This decreases the number of training samples from the *hcp* data set from 3901 to 1610.

The rescaling operation decreases the dynamic range of the outputs. To show this, we first take the output energies (after the aforementioned filtering), and divide them all by the sample with the smallest absolute energy. We then take the logarithm of the absolute value of the results. The same operations are performed on the rescaled energies. Normalized histograms of the results are shown in Fig. 2. Of the original energies, about 95% of the samples lay within a range of five orders of magnitude. After the rescaling, about 94% of the samples lay within a range of only two orders of magnitude. Reducing the dynamic range of the output values greatly improves the model’s prediction of the weak energy samples, which are important at lower densities.

F. Neural Network and Training

We train five neural networks in total. Each is a simple multilayer perceptron, created, trained, and evaluated using PyTorch.²⁰ One of the intended uses for this PES is for Monte Carlo simulations of large collections of *para*-H₂ molecules, where the evaluation of the four-body potential likely dominates the simulation’s runtime. In the recently published paper by Wheatley *et al.* on the four-body PES for helium,⁴³ they noted that the four-body potential requires much more computing time than the two-body or three-body potentials, which limited the

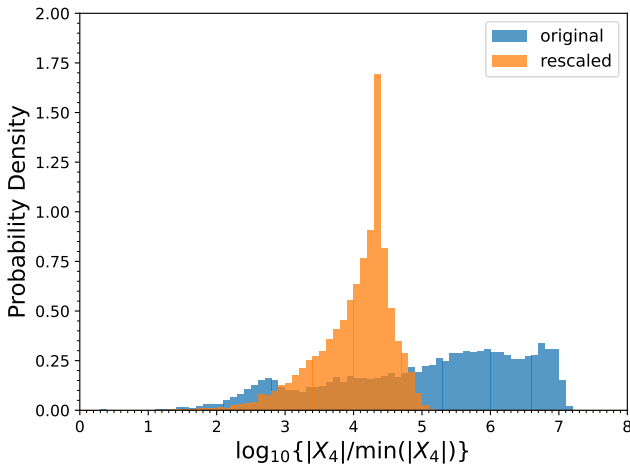


FIG. 2. Normalized histograms of the sample outputs, after dividing them by the smallest value, then taking the absolute value followed by the logarithm. The variable X_4 is a stand-in for either the four-body interaction potential energy V_4 (blue) or the rescaled energy V_4/ϕ (orange), where ϕ is given by Eq. (7) and is evaluated at the appropriate coordinates.

temperatures for which they could perform their PIMC simulations. The model's runtime performance is thus an important factor, and we make reasonable trade-offs concerning other aspects of the network to accommodate it. For example, in addition to large networks, we also create smaller networks that are faster to evaluate, even though they may have larger testing errors.

We create four multilayer perceptrons of different sizes. Each has four hidden layers, alongside the input layer of size 6 and the output layer of size 1. We place ReLU activation functions⁵⁵ between the hidden layers. The four networks are the 64-128-128-64 model (where the first hidden layer has a size of 64, the second has a size of 128, and so on), the 32-64-64-32 model, the 16-32-32-16 model, and the 8-16-16-8 model. A depiction of the 8-16-16-8 model is given in Fig. 3.

We also train a version of the largest network using shifted softplus⁵⁶ activation functions between the layers, which we call the 64-128-128-64-SSP model. Unlike the networks trained with ReLU activation functions, this model is continuously differentiable, for situations where forces are required.

The 16000 *ab initio* samples from the probability distributions are split randomly into training, validation, and testing sets using a 6 : 1 : 1 split, giving 12000 training samples, 2000 validation samples, and 2000 testing samples. The training data is further augmented with the remaining 1610 *ab initio* samples from the *hcp* lattice geometries, *i.e.* those remaining after filtering out all samples with a mean side length greater than 4.5 Å. The input features of each sample are passed through the transformations described in Sec. (II D), and the output energies are rescaled using the transformation described in Sec. (II E).

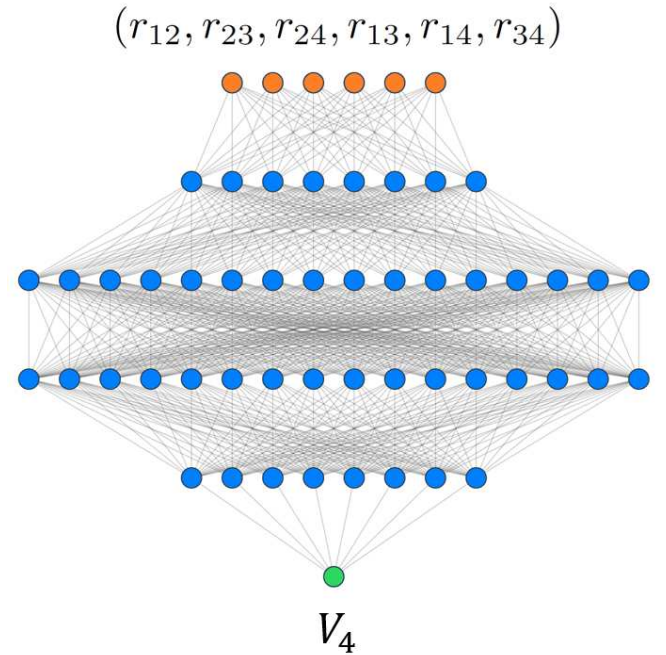


FIG. 3. A depiction of the 8-16-16-8 model. The six orange circles represent the input features. The blue circles represent the fully-connected linear hidden layers. The green circle represents the output. There are a total of 4 ReLU layers, one after each linear layer. The results of the calculations propagate downwards in the figure. Not shown are the feature transformations performed on the six side lengths, or the rescaling transformation performed on the output. Diagram made with the assistance of Ref. [57].

For training, we use a batch size of 64, a mean squared error loss function, and an Adam optimizer with a learning rate of 2×10^{-4} , supplemented with a learning rate scheduler that decreases the learning rate by 1% every 25 epochs past the first 100 epochs. The 64-128-128-64 and 64-128-128-64-SSP models were trained for 20000 epochs, and the other three were trained for 10000 epochs. We find that omitting weight decay entirely improves the model's accuracy, most likely due to the low-noise nature of the electronic structure energies. Both batch normalization and dropout were found to have a negligible effect on training, and so were omitted for the final model.

In Fig. 4, we show the loss as a function of the epoch for the training of the 64-128-128-64 and 64-128-128-64-SSP models. Shown are the results for the training data set, the validation data set, and the training data set with the 1610 samples from the *hcp* lattice removed. In the supplementary material, we show similar figures for the other, smaller models.

For both models shown in Fig. 4, the MSE loss decreases rapidly for all data sets. The large amount of noise in the curves for the earlier epochs can be attributed to the fact that we are viewing the logarithm of the MSE loss. As the scheduler decreases the learning rate, all error curves gradually settle. Both models reach a similar

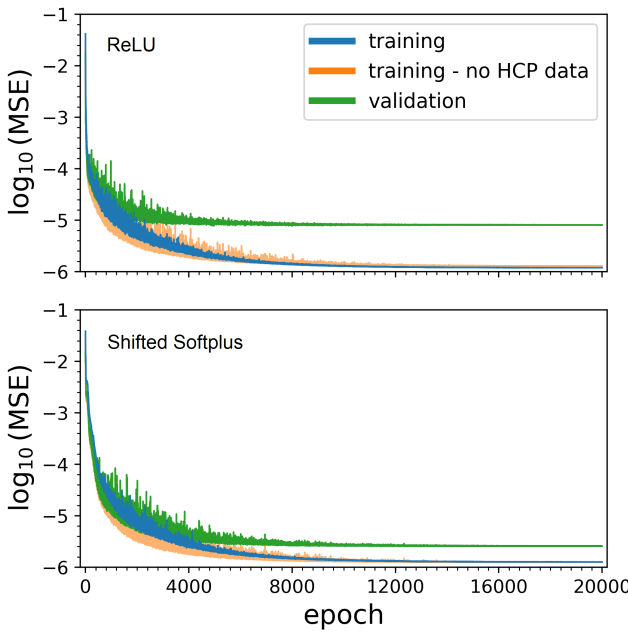


FIG. 4. The base-10 logarithm of the mean squared error loss as a function of the epoch during the training of the 64-128-128-64 model (top), and the 64-128-128-64-SSP model (bottom). The former uses the ReLU activation function, while the latter uses a shifted softplus activation function. The plots are shown for the training data set (blue, solid), the validation data set (green, solid), and the training data set with the 1610 samples from the *hcp* lattice removed (orange, semi-translucent).

training error, but the use of the shifted softplus activation function gives a lower validation error.

The models have a more difficult time fitting the *hcp* lattice samples. In both the 64-128-128-64 and 64-128-128-64-SSP models, the error of the training data exceeds the error of the training data with the *hcp* lattice samples removed, at earlier epochs. The smaller models have even more trouble fitting the *hcp* samples. In the 16-32-32-16 model, the training and validation errors are nearly the same, and in the 8-16-16-8 mode, the training error is *higher* than both the validation error and the error of the training samples with the *hcp*-based samples removed.

At late stage training, the training error becomes nearly constant, and essentially all models beyond a certain epoch can be considered “ideal.” To avoid biasing the models to the test data, we arbitrarily choose each model’s weights corresponding to the very last epoch. The root mean squared errors (RMSE) of the models when compared against the test samples, starting with the 64-128-128-64 and decreasing in size, are 0.120 cm^{-1} , 0.254 cm^{-1} , 0.705 cm^{-1} , and 1.495 cm^{-1} . The RMSE of the 64-128-128-64-SSP model is 0.066 cm^{-1} . As expected, the smaller models produce worse predictions. Using shifted softplus over ReLU as an activation func-

tion for the largest model size roughly halves the RMSE.

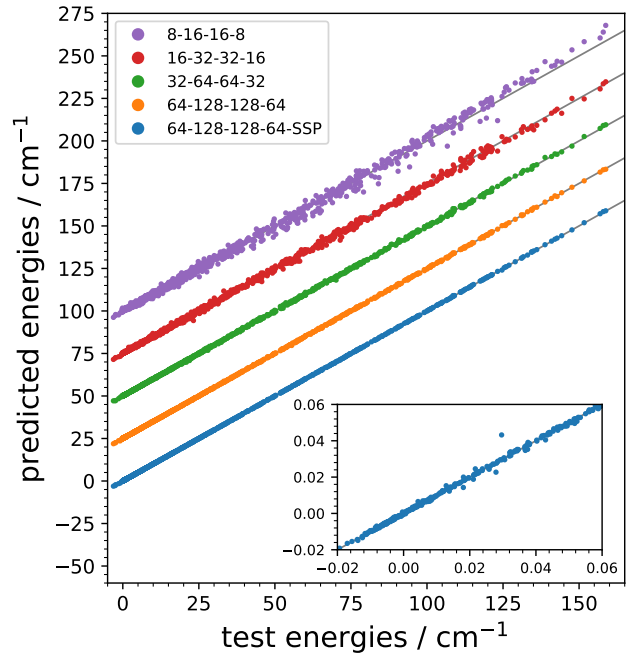


FIG. 5. The four-body interaction energy predicted by each model, plotted against the corresponding true energy, for all samples in the test data set. To avoid overlapping the results, constant offsets are added to the predicted energies of each model. Shown are the outputs for the 64-128-128-64-SSP model (blue) [no offset], the 64-128-128-64 model (orange) [offset by 25 cm^{-1}], the 32-64-64-32 model (green) [offset by 50 cm^{-1}], the 16-32-32-16 model (red) [offset by 75 cm^{-1}], and the 8-16-16-8 model (purple) [offset by 100 cm^{-1}]. The inset shows the predictions for the 64-128-128-64-SSP model for a certain range of weaker energies (both axes in units of cm^{-1}).

In Fig. 5, we show the four-body interaction energy predicted by each model, against the corresponding true energy, for all samples in the test data set. The closer a point is to the diagonal line, the better the prediction. We see that the relatively large 64-128-128-64 and 64-128-128-64-SSP models do an excellent job of predicting the interaction energies in the test set. As we move to smaller models, the predictions become worse. In the inset of Fig. 5, we provide a closer look at the predictions of the 64-128-128-64-SSP model between -0.02 cm^{-1} and 0.06 cm^{-1} . Notably, these predictions are of energies below the model’s RMSE of 0.066 cm^{-1} . Training the models without the energy rescaling procedure described in Sec. (II E) results in much worse predictions of the weak energy samples.

III. DISCUSSION AND ANALYSIS

A. Lebedev Quadrature Comparison

To create the isotropic interaction energies in our PES, we use a 6-point Lebedev quadrature to average over the rotational degrees of freedom of each *para*-H₂ molecule.^{45,51,52} In a Lebedev quadrature, we calculate the interaction energies of the hydrogen molecules in specific combinations of angular orientations, then perform a weighted average of these energies. This weighted average only approximates the true integration over all the rotational degrees of freedom. The 6-point quadrature is described in Sec. (II B).

Using a larger Lebedev quadrature scheme increases the accuracy of the approximation, but also increases the number of terms in the sum. The 6-point Lebedev quadrature scheme is the smallest possible scheme. It uses only 3 angular orientations per molecule, and with 4 molecules, we need $3^4 = 81$ energies to perform a single average. The next largest Lebedev scheme is the 14-point scheme. It uses 7 angular orientations per molecule, and thus requires $7^4 = 2401$ energies to perform a single average, nearly a 30-fold increase over the 6-point scheme.

To estimate the integration error, we select three tetrahedra of different side lengths, and calculate the four-body interaction energies for each one, using both the 6-point and 14-point Lebedev quadrature schemes. The results are shown in Table I. In all three cases, the difference between the 6-point and 14-point averaged energies is acceptably small. Thus, the 6-point Lebedev quadrature scheme should be acceptable for the isotropic energies of our PES.

TABLE I. Interaction energies of four *para*-H₂ molecules in a tetrahedron geometry for three chosen side lengths r , spherically averaged using the 6-point (V_4^{6P}) and 14-point (V_4^{14P}) Lebedev quadratures. Calculations are performed using an AVDZ basis set at the CCSD(T) level.

| r (Å) | V_4^{6P} (cm ⁻¹) | V_4^{14P} (cm ⁻¹) | difference (%) |
|---------|--------------------------------|---------------------------------|----------------|
| 2.20 | 1.9917×10^2 | 1.9887×10^2 | 0.15 |
| 2.95 | 2.3478×10^0 | 2.3484×10^0 | 0.028 |
| 4.00 | -5.9113×10^{-3} | -5.8332×10^{-3} | 1.3 |

B. Basis Set and Method Comparison

The *ab initio* energies in the PES are calculated at the CCSD(T) level of theory, using an AVDZ atom-centred basis with a supplementary (3s3p2d) midbond basis set at the system's centre of mass. Our choice of the calculation method and the size of the basis set takes into account both the quality of the resulting energies and the feasibility and expense of performing the calculations.

To compare the quality of calculations for different methods and basis sets, we calculate the four-body interaction energy of the tetrahedron geometry for side

lengths between 2.2 Å and 4.5 Å. We do so for four different cases: at the HF level of theory using an AVDZ basis, at the MP2 level of theory using an AVDZ basis, at the CCSD(T) level of theory using an AVDZ basis, and at the CCSD(T) level of theory using an AVTZ basis. All calculations also use a supplementary (3s3p2d) basis set at the system's centre of mass. We also show the four-body component of the four-body dispersion interaction potential, also known as the Bade potential (see Sec. (III D)).

The results are shown in Fig. 6. We see that the CCSD(T) energies calculated using both the AVDZ and AVTZ basis sets are qualitatively and quantitatively very similar. The MP2 curve is qualitatively different from both CCSD(T) curves; it is more repulsive overall, and does not have the same “dip” around 3.8 Å. At short ranges, the MP2/AVDZ and CCSD(T)/AVDZ energies differ from the CCSD(T)/AVTZ energies by around 10 % and 2 %, respectively. The HF curve is the most repulsive of all the curves, and shows no dispersion interaction whatsoever at long ranges. The analytic dispersive Bade potential is attractive for the entire range, and also much weaker. At long distances, the CCSD(T)/AVDZ and CCSD(T)/AVTZ curves converge to the Bade potential, which is a good indication of their quality.

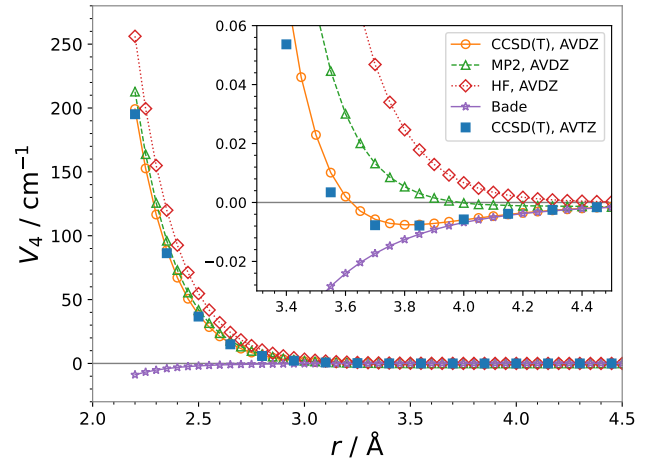


FIG. 6. The four-body interaction potential energies of a tetrahedron, for side lengths between 2.2 Å and 4.5 Å. Shown are the energies calculated for {theory level, basis set} combinations of {CCSD(T), AVDZ} (orange circles), {CCSD(T), AVTZ} (solid blue squares), {MP2, AVDZ} (green triangles), and {HF, AVDZ} (red diamonds), alongside the Bade potential (purple stars). We use the Midzuno-Kihara-type estimate of the Bade coefficient in the Bade potential shown here, although the difference between that estimate and the other estimates isn't visible at this scale.

In Fig. 7, we show the relative error of calculating the four-body interaction energy of a tetrahedron with an AVDZ basis set relative to an AVTZ basis set. The two curves are more similar in form at short distances and at long distances. The relative error naturally worsens

around 3.6 Å, which is roughly where the interaction energies cross 0, as can be seen in Fig. 6.

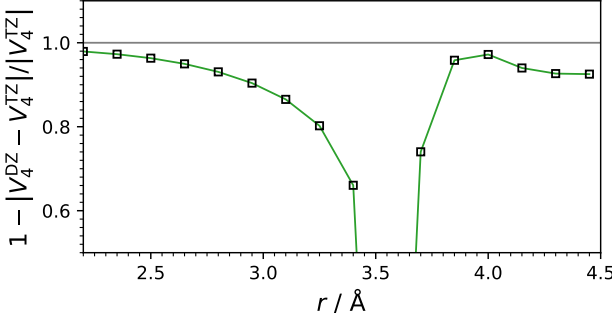


FIG. 7. The relative error of calculating the four-body interaction energy of a tetrahedron with the AVDZ basis set relative to the AVTZ basis set as a function of the tetrahedron's side length r . The dip in the graph occurs around where the four-body energy crosses 0.

Because basis sets are finitely sized, all our calculations experience a systematic basis set size error (BSSE). One way to estimate the BSSE is to perform the same calculation with basis sets of several sizes, and extrapolate the energies to that of an infinitely large basis. We select two common extrapolation functions, the exponential decay function, given by

$$E_e(N) = E_e^{(\infty)} + c_e \exp\{-\alpha N\} \quad (8)$$

and the power decay function, given by

$$E_p(N) = E_p^{(\infty)} + c_p N^{-\beta}. \quad (9)$$

In both equations, N is the basis set cardinality (AVDZ = 2, AVTZ = 3, AVQZ = 4, etc.), $E_e^{(\infty)}$ and $E_p^{(\infty)}$ are the energies for an infinitely large basis set as predicted by the exponential and power decay fits respectively, and c_e , c_p , α , and β are constants.

In Fig. 8, we show the four-body interaction energy of tetrahedra of side lengths 2.2 Å and 2.95 Å as a function of the basis set cardinality, using both extrapolation functions. The fit constants are provided in the supplementary material. For a tetrahedron of side length 2.2 Å (2.95 Å), the AVDZ energy captures 97.9% (90.4%) of the AVTZ energy, 97.1% (88.5%) of the AVQZ energy, 96.6% (88.1%) of the exponentially extrapolated energy, and 95.9% (87.5%) of the power decay extrapolated energy. The power decay function gives a much more pessimistic prediction of the convergence rate than the exponential decay function for the smaller tetrahedron.

The BSSE from using the AVDZ basis set is greater for larger geometries. Similarly, Wheatley *et al.* found that the difference between AVTZ and AVQZ calculations for four-body systems of helium, relative to the energy, increases with the size of the geometry.⁴³ The basis set size error from using an AVDZ basis set exceeds the

fit error from the neural network for the 64-128-128-64 and 64-128-128-64-SSP models. We should also note that, compared to the AVDZ calculations, the AVTZ and AVQZ calculations respectively take an average of 25 and 420 times as long, and require about 4 and 30 times as much memory.

To put these errors into perspective, one important use case for this PES is in numerical simulations of *para*-H₂ molecules alongside the FSH pair potential and the recent three-body PES. The FSH potential predicts a pair interaction energy of 1079.4 cm⁻¹ between two *para*-H₂ molecules 2.2 Å apart. The recent three-body PES predicts a three-body interaction energy of -578.4 cm⁻¹ between three *para*-H₂ molecules in an equilateral triangle of side length 2.2 Å. The four-body interaction energy for a tetrahedron with a side length of 2.2 Å is roughly 200 cm⁻¹. At 2.95 Å, the two-body, three-body, and four-body energies for the aforementioned shapes are 19.0 cm⁻¹, -16.4 cm⁻¹, and about 2.1 cm⁻¹, respectively. Keeping in mind that the four-body interaction is itself typically viewed as a correction term to the two-body and three-body interactions, the BSSE for this PES is probably tolerable for most applications, even at larger geometries.

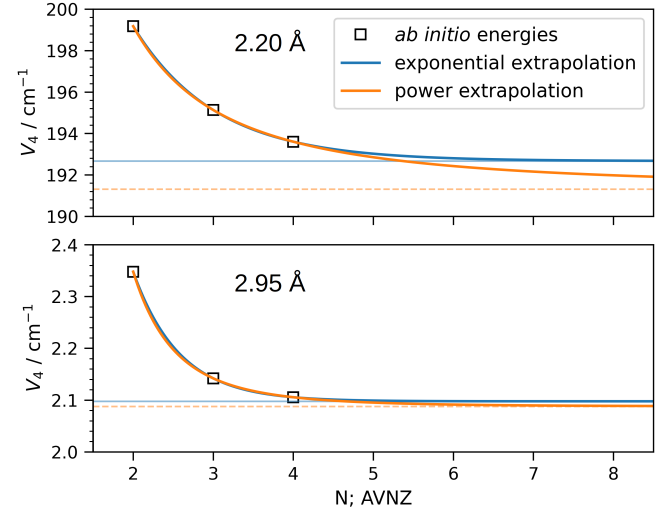


FIG. 8. The four-body interaction energy of a tetrahedron of side length 2.2 Å (top) and of side length 2.2 Å (bottom), as a function of the basis set size (AVDZ = 2, AVTZ = 3, AVQZ = 4, etc.). The energies are extrapolated using the exponential decay extrapolation (blue curve) and the power decay extrapolation (orange curve). The horizontal lines represent the energies when extrapolated to a basis of infinite size.

C. Short Range: Exponential Decay

We have no training samples with a side length less than 2.2 Å, and thus we need a method to extrapolate our energies to smaller geometries.

Consider the function $V_4(\{sr_{ij}\})$, where $\{r_{ij}\}$ denotes the six side lengths with the condition that the shortest among them is 2.2 Å, and $s \approx 1$ is a scalar. By modifying s , we scale all the side lengths by the same factor. The four-body *para*-H₂ interaction energy $V_4(\{sr_{ij}\})$ generally scales exponentially as a function of s . We can see that this is the case for the tetrahedron geometry in Fig. 6. In fact, it is the case for all 8 of the highest energy *hcp* geometries shown in Fig. 9, and the majority of the lower-energy *hcp* geometries as well. Only some of the *hcp* geometries with very weak energies do not fit well as a function of s to the exponential decay function. However, because they are weak, the error from this poor fit is generally insignificant as long as the energies aren't extrapolated to extremely short distances. We use an exponential decay fit to extrapolate the four-body *para*-H₂ interaction PES to geometries where the shortest side length is less than 2.2 Å. The details are provided in the supplementary material.

D. Long Range: Bade Potential

The quadrupole-dipole dispersion potential^{46,47} is

$$V_B(\{\mathbf{r}_i\}) = V_B^{(2)}(\{\mathbf{r}_i\}) + V_B^{(3)}(\{\mathbf{r}_i\}) + V_B^{(4)}(\{\mathbf{r}_i\}) \quad (10)$$

where the “pair component” is given by

$$V_B^{(2)}(\{\mathbf{r}_i\}) = -B_{12} \sum_{i < j}^4 r_{ij}^{-12}, \quad (11)$$

the “triplet component” is given by

$$V_B^{(3)}(\{\mathbf{r}_i\}) = -B_{12} \sum_{j=1}^4 \sum_{i \neq j}^3 \sum_{k > i, k \neq j}^4 \frac{(1 + (\mathbf{u}_{ij} \cdot \mathbf{u}_{jk}))^2}{r_{ij}^6 r_{jk}^6}, \quad (12)$$

and the “quadruplet component” is given by

$$V_B^{(4)}(\{\mathbf{r}_i\}) = -2B_{12}[f(1234) + f(1243) + f(1324)], \quad (13)$$

where

$$\begin{aligned} f(ijkl) = & (r_{ij} r_{jk} r_{kl} r_{li})^{-3} [-1 \\ & + (\mathbf{u}_{ij} \cdot \mathbf{u}_{jk})^2 + (\mathbf{u}_{ij} \cdot \mathbf{u}_{kl})^2 + (\mathbf{u}_{ij} \cdot \mathbf{u}_{li})^2 \\ & + (\mathbf{u}_{jk} \cdot \mathbf{u}_{kl})^2 + (\mathbf{u}_{jk} \cdot \mathbf{u}_{li})^2 + (\mathbf{u}_{kl} \cdot \mathbf{u}_{li})^2 \\ & - 3(\mathbf{u}_{ij} \cdot \mathbf{u}_{jk})(\mathbf{u}_{jk} \cdot \mathbf{u}_{kl})(\mathbf{u}_{kl} \cdot \mathbf{u}_{ij}) \\ & - 3(\mathbf{u}_{ij} \cdot \mathbf{u}_{jk})(\mathbf{u}_{jk} \cdot \mathbf{u}_{li})(\mathbf{u}_{li} \cdot \mathbf{u}_{ij}) \\ & - 3(\mathbf{u}_{ij} \cdot \mathbf{u}_{kl})(\mathbf{u}_{kl} \cdot \mathbf{u}_{li})(\mathbf{u}_{li} \cdot \mathbf{u}_{ij}) \\ & - 3(\mathbf{u}_{jk} \cdot \mathbf{u}_{kl})(\mathbf{u}_{kl} \cdot \mathbf{u}_{li})(\mathbf{u}_{li} \cdot \mathbf{u}_{jk}) \\ & + 9(\mathbf{u}_{ij} \cdot \mathbf{u}_{jk})(\mathbf{u}_{jk} \cdot \mathbf{u}_{kl})(\mathbf{u}_{kl} \cdot \mathbf{u}_{li})(\mathbf{u}_{li} \cdot \mathbf{u}_{ij})]. \end{aligned} \quad (14)$$

In the above equations, B_{12} is a constant, and r_{ij} and \mathbf{u}_{ij} are the distance and unit vector from position \mathbf{r}_i to \mathbf{r}_j , respectively.

To create the long-range correction to our PES, we are only interested in the quadruplet component. This is because when calculating the four-body interaction energy in Eq. (2), the pair and triplet components are already subtracted out. Thus, our analytic long-range interaction will only be Eq. (13), which we refer to as the Bade potential in the remainder of the paper.

At long distances, the Bade potential decays as r^{-12} . We plot the Bade potential alongside the *ab initio* energies in Fig. 6 for tetrahedra of side lengths between 2.2 Å and 4.5 Å. We see that the CCSD(T) curves and the Bade potential converge at long distances. Unlike the *ab initio* energies, the Bade potential is net attractive and much weaker at short range. This discrepancy mirrors the case for the three-body interactions, wherein the ATM potential predicts the short-range energies to be weak and net repulsive, whereas the three-body *ab initio* energies are stronger and attractive.

Estimates of the B_{12} Coefficient

There is much less information in the literature on the interaction coefficient for the four-body dispersion interaction B_{12} than the C_6 coefficient for the pair interaction, or even the C_9 coefficient for the three-body interaction. We can approximate the C_6 , C_9 , and B_{12} using⁴⁶

$$C_6 \approx \frac{3}{4} \hbar \omega_0 \alpha^2 \quad (15)$$

$$C_9 \approx \frac{9}{16} \hbar \omega_0 \alpha^3 \quad (16)$$

$$B_{12} \approx \frac{45}{64} \hbar \omega_0 \alpha^4, \quad (17)$$

where α is the polarizability of molecular hydrogen, and $\hbar \omega_0$ is a coupling constant. Combining these equations gives

$$B_{12} = \frac{5}{3} \frac{C_9^2}{C_6}. \quad (18)$$

This relationship is similar to the Midzuno-Kihara approximation,⁵⁸ which relates C_9 and C_6 through $C_9/C_6 = 3\alpha/4$. Using values of $C_6 = 58203.6 \text{ cm}^{-1} \text{ Å}^6$ from Ref. [59], and $C_9 = 34336.2 \text{ cm}^{-1} \text{ Å}^9$ from Ref. [29], we find an estimate of $B_{12} = 33760.1 \text{ cm}^{-1} \text{ Å}^{12}$. We can also approximate B_{12} directly from the *ab initio* CCSD(T) interaction energies for the tetrahedron geometry. The estimates of B_{12} from energies calculated with the AVDZ and AVTZ basis sets, are $31667.0 \text{ cm}^{-1} \text{ Å}^{12}$ and $29492.8 \text{ cm}^{-1} \text{ Å}^{12}$, respectively (see the supplementary material). The Midzuno-Kihara-like estimate of B_{12} is in surprisingly good agreement with the estimates from the *ab initio* energies, given that it is derived from a combination of three approximations.

For the PES published with this paper, we decide to use the AVTZ-based estimate for B_{12} . We should em-

phasize that the neural network presented with this paper does not depend on the chosen value of B_{12} . Instead, the PES adjusts the interaction energy of a sample at long ranges either after or instead of evaluating the neural network. For cases where the long-range accuracy is especially important, the value of B_{12} can be easily replaced in the code without having to retrain the model.

Transitions Between Different Parts of the PES

With no intervention, there are small discontinuities between the short-range, long-range, and multilayer perceptron parts of the PES. These discontinuities are typically very small, and in situations where only energies are required, are probably not too concerning.

However, there are many situations where it would be desirable to calculate forces with the PES. The Python functor for the PES provided in the accompanying repository wraps around the different parts of the PES introduces continuous transitions between them. When used with the 64-128-128-64-SSP model, this PES is continuously differentiable. The conceptual details of the transition between the short-range, long-range, and multilayer perceptron parts of the PES are provided in the supplementary material.

E. Interactions in Solid Parahydrogen

Solid *para*-H₂ is a hexagonal close-packed (*hcp*) crystal.¹³ Even though solid *para*-H₂ is a quantum solid whose molecules are very delocalized about their nominal lattice sites, we can gain several insights from analyzing its classical frozen lattice configuration.

Earlier, we mentioned generating training data based on the geometries of the *hcp* lattice. We select a reference molecule in the lattice, and generate all four-body geometries involving this reference molecule such that (1) at least one side length is equal to the lattice constant, and (2) no side length is more than twice the lattice constant. Geometries that do not obey these conditions have a nearly negligible contribution to the total interaction energy, even at a lattice constant as low as 2.2 Å. There are 83 distinct four-body shapes that satisfy these conditions, each occurring with a certain frequency. A subset of the geometries are presented in Table II. It shows the six side lengths $\{r_{ij}\}$ of the geometry normalized by the lattice constant, and the number of times it appears subject to the aforementioned conditions N_c . The geometries are listed in order of increasing average side length. The full table with all 83 geometries, including sample energy values is provided in the supplementary material.

Consider a classical frozen *hcp* lattice with a lattice constant of 2.2 Å. For each geometry, we take its four-body *para*-H₂ interaction energy $V_4(\{r_{ij}\})$, multiply it with the number of times that geometry appears N_c , and divide by 4 to account for multiple counting. This gives

us $V_4^{(\text{tot})}$, the total contribution of each geometry to the average four-body *para*-H₂ interaction potential energy per particle in the *hcp* lattice. In Fig. 9, we show $V_4^{(\text{tot})}$ for each geometry ID in Table II.

We see that nearly all the geometries provide a repulsive contribution for the four-body *para*-H₂ interaction energy. We also see that the majority of geometries have nearly no contribution. Of the 8 geometries with a total contribution greater than 300 cm⁻¹, 7 of them have the lowest geometry ID numbers (and thus the shortest average side lengths). However, the average pair distance itself cannot explain the average interaction energy on its own. Consider geometries 15 and 16 in Table II. These two geometries have the same six side lengths but different physical structures (none of the 24 allowed index permutations turn either geometry into the other). At a lattice constant of 2.2 Å, they have drastically different total contributions $V_4^{(\text{tot})}$ of 3.99 cm⁻¹ and 589.18 cm⁻¹, respectively.

The four-body interaction potential for *para*-H₂ shares many features with the four-body interaction potential of helium.⁴³ Both are repulsive at short range. At larger intermolecular separations, the energies are a mix of repulsive and attractive, although the repulsive energies tend to be stronger and cover a larger amount of the coordinate space.

TABLE II. The geometries of the *para*-H₂ molecules in an *hcp* lattice. The first column shows the geometry ID label. The geometries are labelled in order of increasing side length. The second column shows N_c , the number of times that geometry appears in the first two shells. The remaining six columns show the side lengths of the geometries, normalized by the lattice constant. This table only shows 17 of the 83 geometries that satisfy the conditions described in the text. A full table is provided in the supplementary material.

| ID | N_c | r_{12} | r_{13} | r_{14} | r_{23} | r_{24} | r_{34} |
|----|-------|----------|----------|------------|------------|---------------|---------------|
| 0 | 8 | 1 | 1 | 1 | 1 | 1 | 1 |
| 1 | 48 | 1 | 1 | 1 | 1 | 1 | $\sqrt{2}$ |
| 2 | 12 | 1 | 1 | 1 | 1 | 1 | $\sqrt{8/3}$ |
| 3 | 36 | 1 | 1 | 1 | 1 | 1 | $\sqrt{3}$ |
| 4 | 12 | 1 | 1 | $\sqrt{2}$ | $\sqrt{2}$ | 1 | 1 |
| 5 | 144 | 1 | 1 | 1 | 1 | $\sqrt{2}$ | $\sqrt{3}$ |
| 6 | 48 | 1 | 1 | 1 | 1 | $\sqrt{2}$ | $\sqrt{11/3}$ |
| 7 | 24 | 1 | 1 | 1 | $\sqrt{2}$ | $\sqrt{2}$ | $\sqrt{8/3}$ |
| 8 | 72 | 1 | 1 | 1 | 1 | $\sqrt{3}$ | $\sqrt{3}$ |
| 9 | 48 | 1 | 1 | 1 | 1 | $\sqrt{8/3}$ | $\sqrt{11/3}$ |
| 10 | 48 | 1 | 1 | 1 | 1 | $\sqrt{3}$ | $\sqrt{11/3}$ |
| 11 | 96 | 1 | 1 | 1 | 1 | $\sqrt{3}$ | 2 |
| 12 | 24 | 1 | 1 | $\sqrt{2}$ | $\sqrt{2}$ | 1 | $\sqrt{11/3}$ |
| 13 | 24 | 1 | 1 | 1 | $\sqrt{2}$ | $\sqrt{2}$ | 2 |
| 14 | 24 | 1 | 1 | 1 | 1 | $\sqrt{11/3}$ | $\sqrt{11/3}$ |
| 15 | 48 | 1 | 1 | 1 | $\sqrt{2}$ | $\sqrt{3}$ | $\sqrt{3}$ |
| 16 | 144 | 1 | 1 | $\sqrt{2}$ | $\sqrt{3}$ | 1 | $\sqrt{3}$ |

We can look at the impact of many-body interactions in rare gas solids, such as solid helium-4, neon, argon,

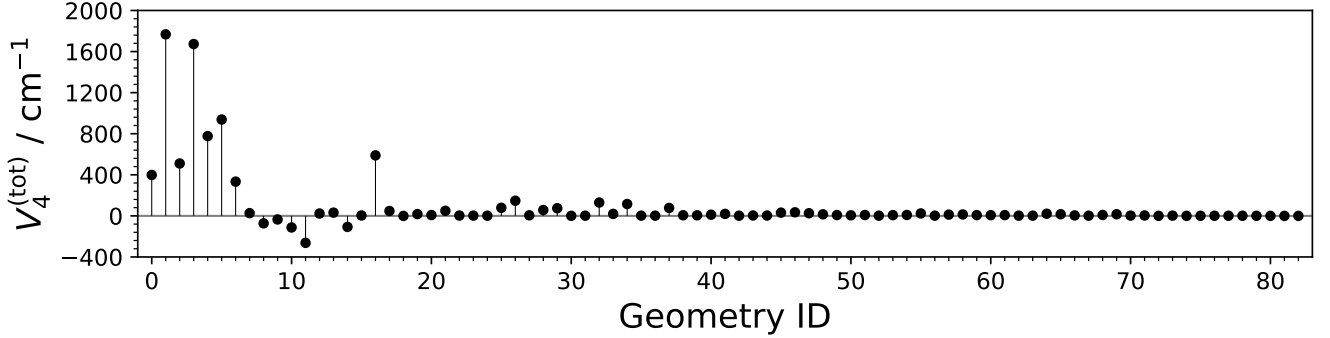


FIG. 9. The total contribution of each geometry to the average four-body *para*-H₂ interaction potential energy per particle in an *hcp* lattice, when the lattice constant is 2.2 Å ($\rho \approx 0.133 \text{ \AA}^{-3}$). The corresponding geometry IDs are provided in the supplementary material. The geometries are labelled in order of increasing average side length.

krypton, and xenon, for insights on how they behave in solid *para*-H₂. Like solid *para*-H₂, the rare gas solids are molecular solids with weak intermolecular dispersion interactions, and are common subjects in quantum path integral simulations.⁶⁰

There appears to be a common pattern in many-body interactions of rare gas atoms. The overall interaction energy at short intermolecular separations switches signs based on the parity of the interaction order. At high densities in solid helium-4, Tian *et al.* found that the 2-body, 4-body, and 6-body interactions have net repulsive contributions, while the 3-body and 5-body interactions have net attractive contributions.⁶¹ The magnitude of the contributions also decrease with every increasing order. Similarly, at high densities in solid krypton, the 2-body and 4-body interactions have overall repulsive contributions, while the 3-body interaction is attractive.⁶² In solid neon, argon, and xenon, the three-body interaction energy is known to be overall attractive.⁶³ It appears that many-body interactions between *para*-H₂ molecules also follow this pattern.

For the equation of state, we calculate the energy per molecule ϵ as a function of the density ρ for a solid *para*-H₂ *hcp* lattice with no zero-point motion. We can then calculate the pressure P as a function of density using

$$P = \rho^2 \frac{\partial \epsilon}{\partial \rho} \Big|_T \quad (19)$$

For these calculations, we use the FSH two-body potential,³¹ the recent isotropic three-body PES,¹⁹ and the 64-128-128-64 four-body PES presented in this paper. In Fig. 10, we show the classical energy-density curves (top) and classical pressure-density curves (bottom), for a lattice whose interactions are made up of the two-body potential on its own (blue, dash-dotted), the two-body and three-body potentials together (orange, dashed), and the two-, three-, and four-body potentials together (green, solid). The top and bottom subfigures both share the same horizontal axis. The highest density shown here, $\rho = 0.1 \text{ \AA}^{-3}$, corresponds to a lattice constant of $a = 2.42 \text{ \AA}$.

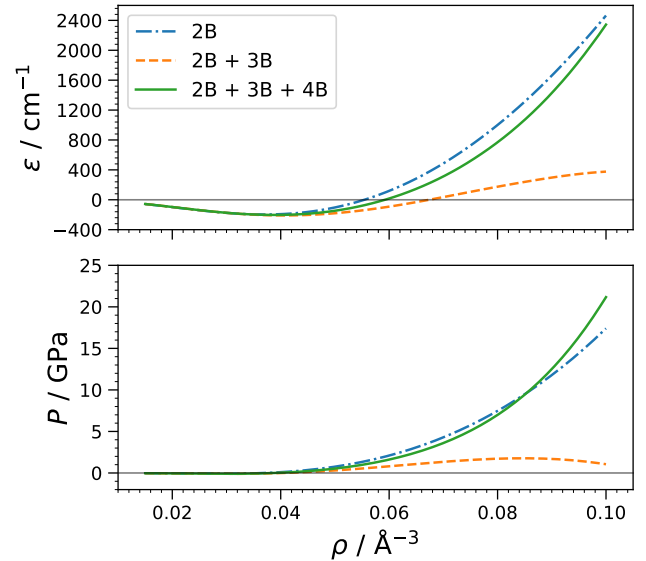


FIG. 10. We show the classical energy-density curves (top) and classical pressure-density curves (bottom), for a frozen *hcp* lattice whose interactions are made up of the two-body potential on its own (blue, dash-dotted), the two-body and three-body potentials together (orange, dashed), and the two-, three-, and four-body potentials together (green, solid). The top and bottom subfigures both share the same horizontal axis. The highest density shown here, $\rho = 0.1 \text{ \AA}^{-3}$, corresponds to a lattice constant of $a = 2.42 \text{ \AA}$.

body and three-body PESs are present. Qualitatively, these results are promising. In an earlier study of PIMC simulations of solid parahydrogen, we found that the pair potential overestimates the pressure-density curve compared to experiment.⁴² However, the inclusion of the three-body potential causes an overcorrection at higher densities,⁴¹ causing the simulation to underestimate the pressure-density curve. Except at very high densities, the four-body potential should place the pressure-density

curve between these two former cases, bringing it closer to experiment.

IV. CONCLUSION

We have presented an isotropic *ab initio* four-body interaction PES for *para*-H₂. The electronic structure calculations are performed at the CCSD(T) level with an AVDZ atom-centred basis set, supplemented by a (3s3p2d) midbond function. The energies are fit to a multilayer perceptron. The procedure used to construct the PES has been provided in detail. This includes the methods of sample generation, the transformations on the input side lengths and the output energies to help improve the training process, and the training of the neural network itself.

We have also discussed how the interaction energy is extrapolated outside the training data's regime, using an analytic dispersion interaction at long intermolecular separations, and an exponential decay when the *para*-H₂ molecules are close together. The four-body *para*-H₂ interaction energy is overall repulsive at high densities. To put this into context, we know from previous PIMC simulations that the *ab initio* two-body FSH PES on its own is too repulsive at high densities,⁴² and that the inclusion of the *ab initio* three-body PES is too attractive at high densities.⁴¹ Using a classical approximation, we show that the additional inclusion of the four-body PES will likely improve the agreement of the simulation results with experiment, except at very high densities.

SUPPLEMENTARY MATERIAL

Refer to the supplementary material for detailed descriptions of the Estimates of Bade Coefficients, Lexicographic Ordering, Training Error Curves for Smaller Models, Short Range Exponential Decay Fit, and Contributions to the *hcp* lattice for each geometry.

ACKNOWLEDGEMENTS

The authors acknowledge the Natural Sciences and Engineering Research Council (NSERC) of Canada (RGPIN-2016-04403), the Ontario Ministry of Research and Innovation (MRI), the Canada Research Chair program (950-231024), and the Canada Foundation for Innovation (CFI) (project No. 35232). A. I. acknowledges the support of the NSERC of Canada (CGSD3-558762-2021).

DATA AVAILABILITY

The data that support the findings of this study are openly available at https://github.com/AlexanderIbrahim1/nن_fourbody_potential/.

The raw inputs and outputs involved in performing the electronic structure calculations for the *ab initio* energies are available at DOI 10.5281/zenodo.11272857.

REFERENCES

- 1 G. R. Medders, A. W. Götz, M. A. Morales, P. Bajaj, and F. Paesani, "On the representation of many-body interactions in water," *J. Chem. Phys.*, vol. 143, p. 104102, 2015.
- 2 Z. Fan, W. Chen, V. Vierimaa, and A. Harju, "Efficient molecular dynamics simulations with many-body potentials on graphics processing units," *Comput. Phys. Commun.*, vol. 218, pp. 10–16, 2017.
- 3 M. Alkan, P. Xu, and M. S. Gordon, "Many-body dispersion in molecular clusters," *J. Phys. Chem. A*, vol. 123, pp. 8406–8416, 2019.
- 4 A. O. de-la Roza, L. M. LeBlanc, and E. R. Johnson, "What is "many-body" dispersion and should I worry about it?," *Phys. Chem. Chem. Phys.*, vol. 22, pp. 8266–8276, 2020.
- 5 M. J. Elrod and R. J. Saykally, "Many-body effects in intermolecular forces," *Chem. Rev.*, vol. 94, p. 1975, 1994.
- 6 G. A. Cisneros, K. T. Wikfeldt, L. Ojamäe, J. Lu, Y. Xu, H. Toraibafard, A. P. Bartók, G. Csányi, V. Molinero, and F. Paesani, "Modeling molecular interactions in water: From pairwise to many-body potential energy functions," *Chem. Rev.*, vol. 116, pp. 7501–7528, 2016.
- 7 H. P. Gush, W. F. J. Hare, E. J. Allin, and H. L. Welsh, "The infrared fundamental band of liquid and solid hydrogen," *Can. J. Phys.*, vol. 38, p. 176, 1960.
- 8 L. H. Nosanow, "Theory of quantum crystals," *Phys. Rev.*, vol. 146, p. 120, 1966.
- 9 O. Bostanjoglo and R. Kleinschmidt, "Crystal structure of hydrogen isotopes," *J. Chem. Phys.*, vol. 46, p. 2004, 1967.
- 10 J. van Kranendonk, *Solid hydrogen: Theory of the properties of solid H₂, HD, and D₂*. Boston, MA: Springer, 1983.
- 11 F. Fernandez-Alonso, C. Cabrillo, R. Fernández-Perea, F. J. Bermejo, M. A. González, C. Mondelli, and E. Farhi, "Solid *para*-hydrogen as the paradigmatic quantum crystal: Three observables probed by ultrahigh-resolution neutron spectroscopy," *Phys. Rev. B*, vol. 86, p. 144524, 2012.
- 12 M. Dusseault and M. Boninsegni, "Atomic displacements in quantum crystals," *Phys. Rev. B*, vol. 95, p. 104518, 2017.
- 13 I. F. Silvera, "The solid molecular hydrogens in the condensed phase: Fundamentals and static properties," *Rev. Mod. Phys.*, vol. 52, p. 393, 1980.
- 14 M. Zoppi and M. Neumann, "PIMC simulations of solid parahydrogen," *Phys. Rev. B*, vol. 43, no. 13, p. 10242, 1991.
- 15 D. Ceperley, "Path integrals in the theory of condensed helium," *Rev. Mod. Phys.*, vol. 67, p. 279, 1995.
- 16 P. Wind and I. Roøggen, "Ab initio calculation of three-body interaction in the (H₂)₃ trimer," *Chem. Phys.*, vol. 211, pp. 179–189, 1996.
- 17 R. J. Hinde, "Three-body interactions in solid parahydrogen," *Chem. Phys. Lett.*, vol. 460, pp. 141–145, 2008.
- 18 S. Manzhos, K. Nakai, and K. Yamashita, "Three-body interactions in clusters CO-(pH₂)_n," *Chem. Phys. Lett.*, vol. 493, pp. 229–233, 2010.
- 19 A. Ibrahim and P.-N. Roy, "Three-body potential energy surface for *para*-hydrogen," *J. Chem. Phys.*, vol. 156, p. 044301, 2022.
- 20 A. Paszke, S. Gross, F. Massa, A. Lerer, J. Bradbury, G. Chanan, T. Killeen, Z. Lin, N. Gimelshein, L. Antiga, A. Desmaison, A. Kopf, E. Yang, Z. DeVito, M. Raison, A. Tejani, S. Chilamkurthy, B. Steiner, L. Fang, J. Bai, and S. Chintala, "PyTorch: an imperative style, high-performance deep learning library," in *Advances in Neural Information Processing Systems* 32, pp. 8024–8035, Curran Associates, Inc., 2019.

²¹M. Abadi, A. Agarwal, P. Barham, E. Brevdo, Z. Chen, C. Citro, G. S. Corrado, A. Davis, J. Dean, M. Devin, S. Ghemawat, I. Goodfellow, A. Harp, G. Irving, M. Isard, Y. Jia, R. Jozefowicz, L. Kaiser, M. Kudlur, J. Levenberg, D. Mané, R. Monga, S. Moore, D. Murray, C. Olah, M. Schuster, J. Shlens, B. Steiner, I. Sutskever, K. Talwar, P. Tucker, V. Vanhoucke, V. Vasudevan, F. Viégas, O. Vinyals, P. Warden, M. Wattenberg, M. Wicke, Y. Yu, and X. Zheng, “TensorFlow: Large-scale machine learning on heterogeneous systems,” 2015. Software available from tensorflow.org.

²²J. O. Hirschfelder, R. B. Bird, and E. L. Spotz, “The transport properties for non-polar gases,” *J. Chem. Phys.*, vol. 16, no. 10, p. 968, 1948.

²³E. A. Mason and W. E. Rice, “The intermolecular potentials of helium and hydrogen,” *J. Chem. Phys.*, vol. 22, no. 5, p. 522, 1954.

²⁴J. M. Farrer and Y. T. Lee, “Intermolecular potentials from crossed beam differential elastic scattering measurements. VII para-H₂ + para-H₂,” *J. Chem. Phys.*, vol. 57, no. 12, p. 5492, 1972.

²⁵I. F. Silvera and V. V. Goldman, “The isotropic intermolecular potential for H₂ and D₂ in the solid and gas phases,” *J. Chem. Phys.*, vol. 69, p. 4209, 1978.

²⁶U. Buck, F. Huisken, A. Kohlhase, D. Otten, and J. Schaefer, “State resolved rotational excitation in D₂ + H₂ collisions,” *J. Chem. Phys.*, vol. 78, p. 4439, 1978.

²⁷M. J. Norman, R. O. Watts, and U. Buck, “A spherical potential for hydrogen from solid state and scattering data,” *J. Chem. Phys.*, vol. 81, p. 3500, 1984.

²⁸P. Diep and J. K. Johnson, “An accurate H₂–H₂ interaction potential from first principles,” *J. Chem. Phys.*, vol. 112, no. 10, p. 4465, 2000.

²⁹R. J. Hinde, “A six-dimensional H₂–H₂ potential energy surface for bound state spectroscopy,” *J. Chem. Phys.*, vol. 128, p. 154308, 2008.

³⁰K. Patkowski, W. Cencek, P. Jankowski, K. Szalewicz, J. B. Mehl, G. Garberoglio, and A. H. Harvey, “Potential energy surface for interactions between two hydrogen molecules,” *J. Chem. Phys.*, vol. 129, p. 094304, 2008.

³¹N. Faruk, M. Schmidt, H. Li, R. J. Le Roy, and P.-N. Roy, “First-principles prediction of the Raman shifts in parahydrogen clusters,” *J. Chem. Phys.*, vol. 141, p. 014310, 2014.

³²T. Omiyinka and M. Boninsegni, “Pair potentials and equation of state of solid *para*-hydrogen to megabar pressure,” *Phys. Rev. B*, vol. 88, p. 024112, 2013.

³³F. Operetto and F. Pederiva, “Diffusion Monte Carlo study of the equation of state of solid para-H₂,” *Phys. Rev. B*, vol. 73, p. 184124, 2006.

³⁴B. M. Axilrod and E. Teller, “Interaction of the van der Waals type between three atoms,” *J. Chem. Phys.*, vol. 11, p. 299, 1943.

³⁵Y. Muto, “Force between nonpolar molecules,” *J. Phys. Math. Soc. Jpn.*, vol. 17, p. 629, 1943.

³⁶F.-M. Tao and Y.-K. Pan, “Møller-Plesset perturbation investigation of the He₂ potential and the role of midbond basis functions,” *J. Chem. Phys.*, vol. 97, no. 7, p. 4989, 1992.

³⁷T. Hollebeek, T.-S. Ho, H. Rabitz, and L. B. Harding, “Construction of reproducing kernel Hilbert space potential energy surfaces for the 1 A” and 1 A’ states of the reaction N(²D) + H₂,” *J. Chem. Phys.*, vol. 114, p. 3945, 2001.

³⁸T.-S. Ho and H. Rabitz, “Reproducing kernel Hilbert space interpolation methods as a paradigm of high dimensional model representations: Application to multidimensional potential energy surface construction,” *J. Chem. Phys.*, vol. 119, no. 13, p. 6433, 2003.

³⁹O. T. Unke and M. Meuwly, “Toolkit for the construction of reproducing kernel-based representations of data: Application to multidimensional potential energy surfaces,” *J. Chem. Inf. Model.*, vol. 57, p. 1923, 2017.

⁴⁰O. T. Unke, S. Chmiela, H. E. Sauceda, M. Gastegger, I. Poltavsky, K. T. Schütt, A. Tkatchenko, and K.-R. Müller, “Machine learning force fields,” *Chem. Rev.*, vol. 121, pp. 10142–10186, 2021.

⁴¹A. Ibrahim and P.-N. Roy, “Equation of state of solid parahydrogen using *ab initio* two-body and three-body interaction potentials,” *J. Chem. Phys.*, vol. 157, p. 174503, 2022.

⁴²A. Ibrahim, L. Wang, T. Halverson, R. J. Le Roy, and P.-N. Roy, “Equation of state and first principles prediction of the vibrational matrix shift of solid parahydrogen,” *J. Chem. Phys.*, vol. 151, p. 244501, 2019.

⁴³R. J. Wheatley, G. Garberoglio, and A. H. Harvey, “Four-body nonadditive potential energy surface and the fourth virial coefficient of helium,” *J. Chem. Eng. Data.*, vol. 68, pp. 3257–3264, 2023.

⁴⁴R. S. Graham and R. J. Wheatley, “Machine learning for non-additive intermolecular potentials: Quantum chemistry to first-principles predictions,” *Chem. Commun.*, vol. 58, p. 6898, 2022.

⁴⁵V. I. Lebedev, “Quadratures on a sphere,” *Zh. Vychisl. Mat. Mat. Fiz.*, vol. 16, no. 2, pp. 293–306, 1976.

⁴⁶W. L. Bade, “Drude-model calculation of dispersion forces. I. General theory,” *J. Chem. Phys.*, vol. 27, pp. 1280–1284, 1957.

⁴⁷W. L. Bade, “Drude-model calculation of dispersion forces. III. The fourth-order contribution,” *J. Chem. Phys.*, vol. 28, pp. 282–284, 1958.

⁴⁸Z. Rolik, L. Szegedy, I. Ladjánszki, B. Ladóczki, and M. Kállyay, “An efficient linear-scaling CCSD(T) method based on local natural orbitals,” *J. Chem. Phys.*, vol. 139, p. 094105, 2013.

⁴⁹K. Raghavachari, G. W. Trucks, J. A. Pople, and M. Head-Gordon, “A fifth-order perturbation comparison of electron correlation theories,” *Chem. Phys. Lett.*, vol. 157, no. 6, pp. 479–483, 1989.

⁵⁰S. F. Boys and F. Bernardi, “The calculation of small molecular interactions by the differences of separate total energies. Some procedures with reduced errors,” *Mol. Phys.*, vol. 19, no. 4, p. 553, 1970.

⁵¹A. D. Becke, “A multicenter numerical integration scheme for polyatomic molecules,” *J. Chem. Phys.*, vol. 88, no. 4, p. 2547, 1988.

⁵²X.-G. Wang and T. Carrington, Jr., “Using Lebedev grids, sine spherical harmonics, and monomer contracted basis functions to calculate being energy levels of HF trimer,” *J. Theor. Comp. Chem.*, vol. 2, no. 4, pp. 599–608, 2003.

⁵³G. Garberoglio, “On the contribution of non-additive three-body interactions to the third virial coefficient of *para*-hydrogen,” *Chem. Phys. Lett.*, vol. 557, p. 26, 2012.

⁵⁴B. T. Fang, “Trilateration and extension to global positioning system navigation,” *J. Guid. Control Dyn.*, vol. 9, pp. 715–717, 1986.

⁵⁵K. Fukushima, “Cognitron: A self-organizing multilayered neural network,” *Biol. Cybernetics*, vol. 20, pp. 121–136, 1975.

⁵⁶K. T. Schütt, H. E. Sauceda, P.-J. Kindermans, A. Tkatchenko, and K.-R. Müller, “SchNet: A deep learning architecture for molecules and materials,” *J. Chem. Phys.*, vol. 148, p. 241722, 2018.

⁵⁷A. LeNail, “NN-SVG: Publication-ready neural network architecture schematics,” *J. Open Source Softw.*, vol. 4, p. 747, 2019.

⁵⁸Y. Midzuno and T. Kihara, “Non-additive intermolecular potential in gases I. van der Waals interactions,” *J. Phys. Soc. Jpn.*, vol. 11, no. 10, pp. 1045–1049, 1956.

⁵⁹M. Schmidt, J. M. Fernández, N. Faruk, M. Nooijen, R. J. Le Roy, J. H. Morilla, G. Tejeda, S. Montero, and P.-N. Roy, “Raman vibrational shifts of small clusters of hydrogen isotopologues,” *J. Phys. Chem. A*, vol. 119, p. 12551, 2015.

⁶⁰C. P. Herrero and R. Ramirez, “Path-integral simulation of solids,” *J. Phys. Condens. Matter*, vol. 26, p. 233201, 2014.

⁶¹C.-L. Tian, F.-S. Liu, F.-Q. Jing, and L.-C. Cai, “Five- and six-body effects on equation of state of solid ⁴He,” *J. Phys. Condens. Matter*, vol. 18, pp. 8103–8112, 2006.

⁶²C.-L. Tian, N. Wu, F. Liu, S. K. Saxena, and X. Zheng, “Four-body interaction energy for compressed solid krypton from quantum theory,” *J. Chem. Phys.*, vol. 137, p. 044108, 2012.

⁶³K. Rościszewski, B. Paulus, P. Fulde, and H. Stoll, “*Ab initio* coupled-cluster calculations for the fcc and hcp structures of rare-gas solids,” *Phys. Rev. B*, vol. 62, no. 9, p. 5482, 2000.

Supplementary Material for: A neural network-based four-body potential energy surface for parahydrogen

Alexander Ibrahim^{1,2} and Pierre-Nicholas Roy^{2, a)}

¹⁾Department of Physics and Astronomy, University of Waterloo, 200 University Avenue West, Waterloo, Ontario N2L 3G1, Canada

²⁾Department of Chemistry, University of Waterloo, 200 University Avenue West, Waterloo, Ontario N2L 3G1, Canada

I. TRILATERATION

In the sample generation procedure, we sample the six side lengths of the geometry

$$(r_{12}, r_{13}, r_{14}, r_{23}, r_{24}, r_{34})$$

and use a trilateration procedure to generate the Cartesian coordinates. The function `SixSideLengthsToCartesian` below accepts the six side lengths of the four-body geometry, and a small number $\varepsilon > 0$ to help account for a corner case involving the position of point 3 (described later). If the six side lengths represent a valid four-body geometry, the function returns four Cartesian coordinates that generate the geometry. Otherwise, the function returns `None`.

```
function SIXSIDELENGTHSTOCARTESIAN(r12, r13, r14, r23, r24, r34, ε)
    ▷ calculate the relevant x positions
    x2 ← r12
    x3 ← (r122 + r132 - r232) / 2r12
    x4 ← (r142 - r242 + r122) / 2r12

    ▷ calculate the y positions, accounting for a corner case and floating-point errors
    y32 ← r132 - x32

    ▷ indication that the geometry is impossible
    if y32 < 0 and |y32| > ε then
        return None
    end if

    if y32 > ε then
        y3 ← √y32
        y4 ← (r142 - r342 + r132 - 2x3x4) / 2y3
    else
        y3 ← 0
        y4 ← 0
    end if

    ▷ calculate z4, accounting for floating-point errors
    z42 ← r142 - x42 - y42

    ▷ indication that the geometry is impossible
    if z42 < 0 and |z42| > ε then
        return None
    end if

    z4 ← √max(0, z42)

    ▷ All coordinates needed to generate the points have been calculated
```

^{a)}Electronic mail: pnroy@uwaterloo.ca

```

 $(p_1, p_2, p_3, p_4) \leftarrow \{(0, 0, 0), (x_2, 0, 0), (x_3, y_3, 0), (x_4, y_4, z_4)\}$ 
return  $(p_1, p_2, p_3, p_4)$ 
end function

```

Using this procedure, the generated points satisfy certain properties. Point 1 is always at the origin. Point 2 lies on the positive x -axis. Point 3 lies in the region $y \geq 0$ and $z = 0$. Point 4 lies in the region $z \geq 0$. The two conditional statements that cause the function to return **None** are those in which the six side lengths do not correspond to a valid geometry. They indicate that the six side lengths violate the triangle inequality rule in one or more ways. In the general case where point 3 lies in the xy -plane but not on the x -axis, the procedure can assign point 4 a definite, unique position. However, if point 3 lies on the x -axis and $y_3 = 0$, the calculation for y_4 blows up. In this special case, points 1, 2, and 3 all lie on the x -axis, and point 4 may lie anywhere on a ring of radius $\sqrt{r_{14}^2 - x_4^2}$ that lies parallel to the yz -plane and is centred at x_4 on the x -axis. We may arbitrarily select $y_4 = 0$ without modifying the relative pair distances of the system. Calculating y_3 and z_4 each involve taking a square root, and in cases where y_3 and z_4 are very close to or essentially 0, floating-point errors can cause the arguments to the square root to be negative. The above function accounts for these cases.

II. ESTIMATES OF BADE COEFFICIENTS

In Fig. 1, we plot transformed versions of the Bade potential alongside the *ab initio* CCSD(T) AVDZ and AVTZ interaction energies for a tetrahedron as a function of the tetrahedron side length r . For the transformations, we multiply the interaction energies by r^{12} , and rescale all the curves by the same constant such that the transformed Bade potential is equal to -1 . The figure makes it easier to see that the *ab initio* energies have the expected r^{-12} decay rate at large intermolecular separations. It is from where these rescaled curves level out that we estimate the interaction coefficients B_{12} derived from the AVDZ and AVTZ *ab initio* energies.

III. LEXICOGRAPHIC ORDERING

Lexicographic ordering is a way to compare two ordered sequences based on their elements. For readers familiar with the Python programming language, this is the kind of ordering that Python uses to compare two tuples of numbers. When comparing two sequences, we compare elements at the same index in either sequence, from left to right. If the two elements are equal, we move on to compare the elements in the next index. As soon as we hit an index where one element is lower than the other, the sequence of the lower element is considered the lower sequence overall. In terms of pseudocode, this can be represented as the following function **LexLowest**, which takes two sequences, compares them lexicographically, and returns the smallest of the two (or either if they are equal).

```

function LEXLOWEST( $A, B$ )
   $n \leftarrow$  length of  $A$ 
  for  $i \leftarrow 1$  to  $n$  do
    if  $A[i] < B[i]$  then
      return  $A$ 
    else if  $A[i] > B[i]$  then
      return  $B$ 
    end if
  end for
  return  $A$             $\blacktriangleright$   $A$  and  $B$  are equal, return either
end function

```

For example, suppose we have input samples

$$\begin{aligned}
s_0 &= (2, 3, 4, 5, 6, 7) \\
s_1 &= (2, 3, 4, 7, 1, 9) \\
s_2 &= (1, 9, 11, 25, 13, 15).
\end{aligned}$$

When comparing these samples, we would find that $\text{LexLowest}(s_0, s_1) = s_0$, because of the comparison of 5 and 7 in the fourth position, $\text{LexLowest}(s_0, s_2) = s_2$, because of the comparison of 2 and 1 in the first position, and $\text{LexLowest}(s_1, s_2) = s_2$, again because of the comparison of 2 and 1 in the first position.

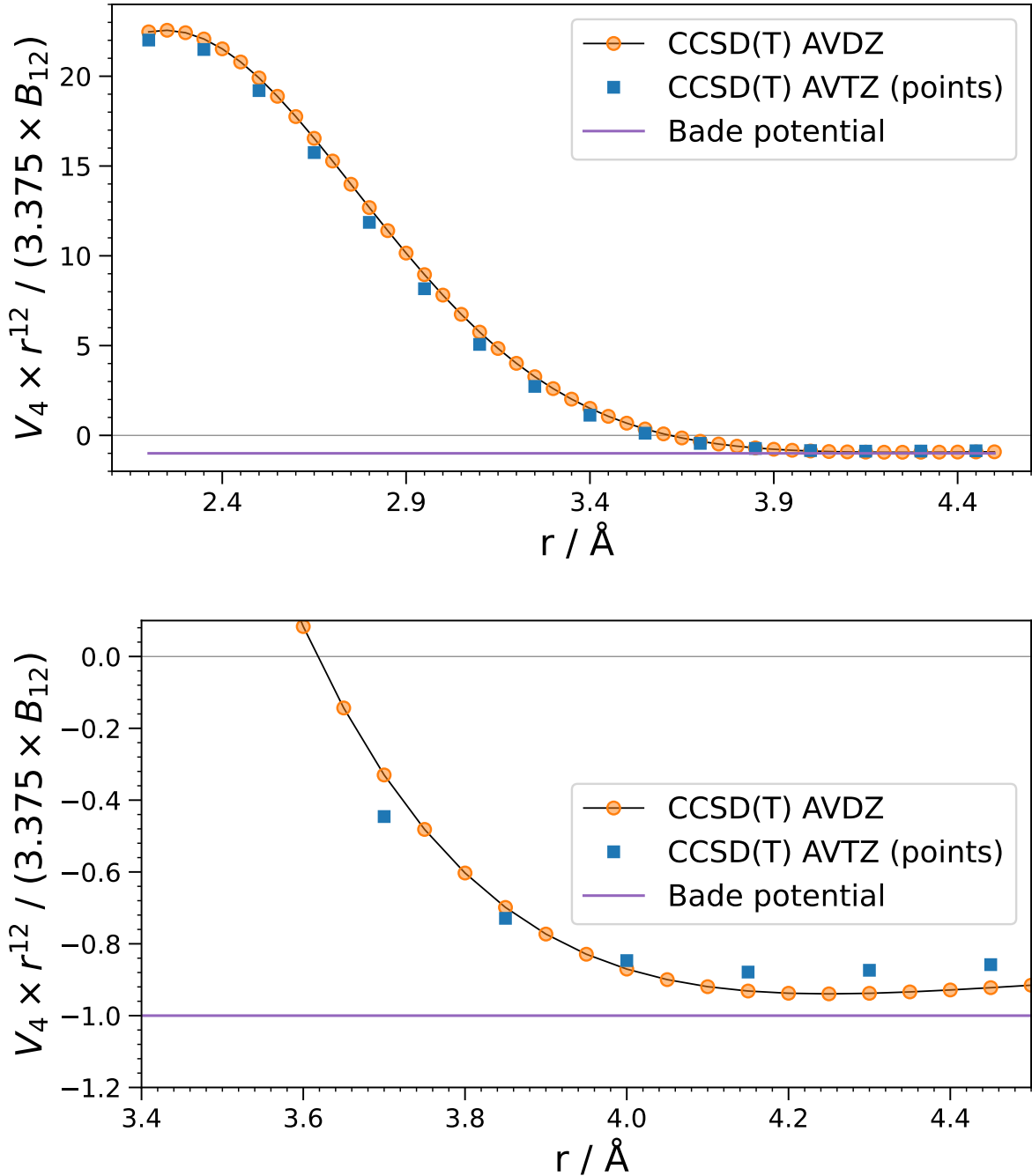


FIG. 1. The rescaled four-body interaction energy for a tetrahedron geometry, as a function of the tetrahedron's side length r . Shown are the CCSD(T) energies calculated using the AVDZ basis (orange circles, black line), and the AVTZ basis (blue squares), as well as the Bade potential (purple line). The term in the y -axis label, B_{12} , is the Bade coefficient as estimated using the Midzuno-Kihara-inspired approximation. The top subfigure shows the results for the entire range of energies calculated for the tetrahedron, while the bottom subfigure emphasizes the region where the long-range r^{-12} decay begins.

IV. TRAINING ERROR CURVES FOR SMALLER MODELS

The main text contains the training error of the neural network as a function of epoch, for the 64-128-128-64 model. Here we show the training curves for the 32-64-64-32 model (Fig. 2), the 16-32-32-16 model (Fig. 3), and the 8-16-16-8

model (Fig. 4).

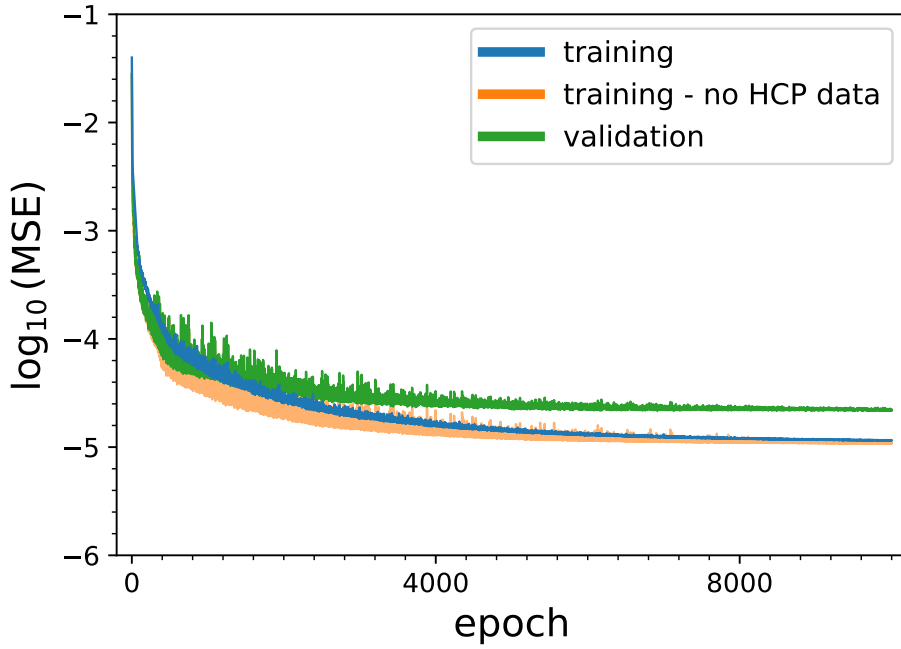


FIG. 2. The base-10 logarithm of the mean squared error loss as a function of the epoch during the training of the 32-64-64-32 model. The plots are shown for the training data set (blue, solid), the validation data set (green, solid), and the training data set with the 1610 samples from the *hcp* lattice removed (orange, semi-translucent).

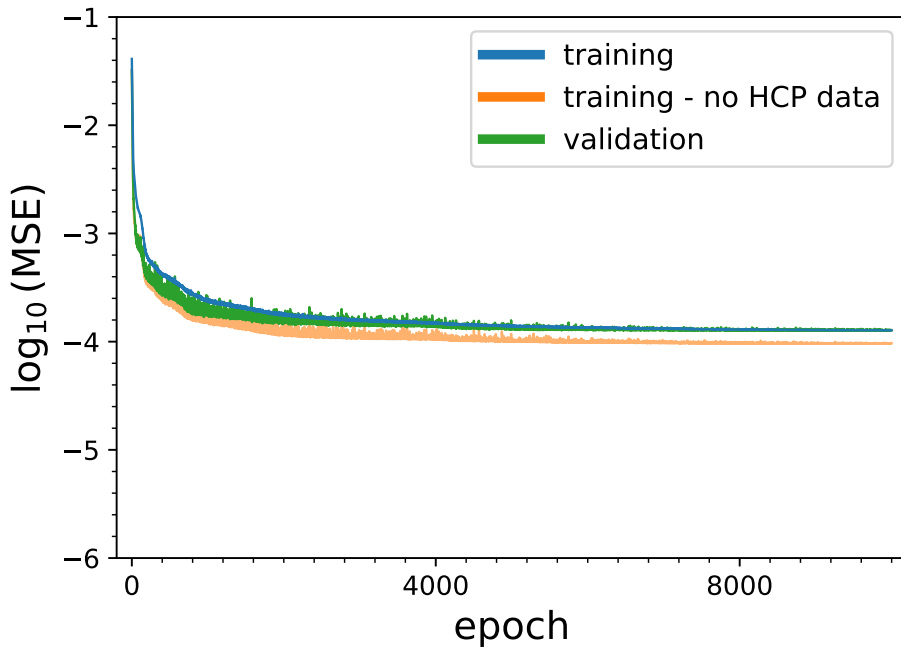


FIG. 3. The base-10 logarithm of the mean squared error loss as a function of the epoch during the training of the 16-32-32-16 model. The plots are shown for the training data set (blue, solid), the validation data set (green, solid), and the training data set with the 1610 samples from the *hcp* lattice removed (orange, semi-translucent).

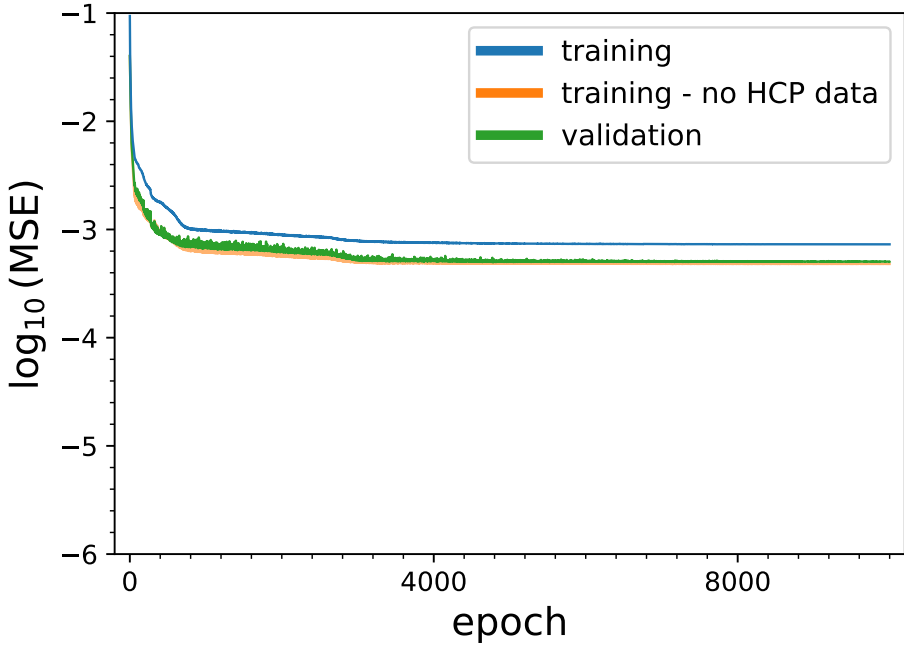


FIG. 4. The base-10 logarithm of the mean squared error loss as a function of the epoch during the training of the 8-16-16-8 model. The plots are shown for the training data set (blue, solid), the validation data set (green, solid), and the training data set with the 1610 samples from the *hcp* lattice removed (orange, semi-translucent).

V. BASIS SET SUPERPOSITION ERROR FIT CONSTANTS

In the Discussion and Analysis section of the main text, in the subsection titled “Basis Set and Method Comparison”, we take the AVDZ, AVTZ, and AVQZ energies for tetrahedra and extrapolate them to infinite basis size using the the exponential decay function

$$E_e(N) = E_e^{(\infty)} + c_e \exp\{-\alpha N\} \quad (1)$$

and the power decay function

$$E_p(N) = E_p^{(\infty)} + c_p N^{-\beta}. \quad (2)$$

For the tetrahedron of side length 2.2 Å, the fit constants are $E_e^{(\infty)} = 192.668 \text{ cm}^{-1}$, $c_e = 45.341 \text{ cm}^{-1}$, $\alpha = 0.9707$, $E_p^{(\infty)} = 191.311 \text{ cm}^{-1}$, $c_p = 26.999 \text{ cm}^{-1}$, and $\beta = 1.780$. For the tetrahedron of side length 2.95 Å, the fit constants are $E_e^{(\infty)} = 2.0976 \text{ cm}^{-1}$, $c_e = 7.954 \text{ cm}^{-1}$, $\alpha = 1.729$, $E_p^{(\infty)} = 2.0875 \text{ cm}^{-1}$, $c_p = 3.775 \text{ cm}^{-1}$, and $\beta = 3.858$.

VI. SHORT RANGE: EXPONENTIAL DECAY FIT

For four-body geometries with at least one side length shorter than 2.2 Å, we use an extrapolation function that is a linear combination of an exponential decay fit and a linear fit. For well-behaved cases, the extrapolation function is entirely the exponential decay fit. For cases where the exponential decay fit would behave poorly or blow up, the linear fit becomes more prominent.

Suppose we have a geometry g , made up of the six side lengths $g = \{r_{ij}\}$, where at least one of the side lengths is less than 2.25 Å. Define $\Delta R = 0.01 \text{ \AA}$ and $\tilde{R}_U = 2.25 \text{ \AA}$, where the subscript is chosen in the context of a later section in the supplementary material. Let R_0 be the shortest side length in the input. We calculate the scaling factors $s_0 = \tilde{R}_U/R_0$ and $s_1 = (\tilde{R}_U + \Delta R)/R_0$, and define two new geometries $g_0 = \{s_0 r_{ij}\}$ and $g_1 = \{s_1 r_{ij}\}$.

We now calculate the exponential coefficient

$$c = \frac{1}{\Delta R} \ln \left| \frac{V_4(g_1)}{V_4(g_0)} \right|. \quad (3)$$

The energy for the original geometry g is now calculated using the exponential decay fit

$$V_4^{(\text{ex})}(g) = V_4(g_0) \exp\{-c(\tilde{R}_U - R_0)\}. \quad (4)$$

However, there are cases where c is very large, and Eq. (4) blows up very quickly. On closer inspection, this typically only happens in cases where $V_4(g_0)$ is very close to 0, which means a small absolute change in energy results in a large relative change in energy. To prevent this, we smoothly transition from the exponential fit to a less physically realistic, but more numerically stable linear fit.

The full equation is

$$V_4(g) = \omega(c; c', c'')V_4^{(\text{ex})}(g) + [1 - \omega(c; c', c'')]V_4^{(\text{li})}(g) \quad (5)$$

where $V_4^{(\text{li})}(g)$ is a linear extrapolation below $r = r_0$, $c' = 6$, $c'' = 8$, and $\omega(x; a, b)$ is given by

$$\omega(x; a, b) = \begin{cases} 0 & \text{if } x \leq a, \\ \frac{1}{2}[1 - \cos(\pi k)] & \text{if } a < x < b, \\ 1 & \text{if } x \geq b \end{cases} \quad (6)$$

where $k = (x - a)/(b - a)$. If c is below c' , the fit is entirely exponential; if c is above c'' , the fit is entirely linear; and if c is between them, it is a finite linear combination of the two. The constants c' and c'' are chosen by hand after investigating certain cases where the exponential decay fit behaved poorly. The linear fit purposely sacrifices accuracy for stability. However, because the calculation of the exponential coefficient only blows up when the energies involved are weak, the error from this linear adjustment is generally insignificant as long as the energies aren't extrapolated to extremely short distances. The decision to set \tilde{R}_U to 2.25 Å rather than 2.2 Å is done in anticipation of the use of a transition function described in the next section.

VII. TRANSITIONS BETWEEN DIFFERENT PARTS OF THE PES

Description

The PES, using the MLP trained with the shifted softplus activation function, is continuously differentiable.

Transition between *ab initio* and dispersive parts

Conceptually, the PES is split into an “*ab initio* part,” a “dispersive part,” and a “mixed (*ab initio*/dispersive) part.” The *ab initio* part is made of the multilayer perceptron (MLP) and the exponential decay parts, described in further detail later. The dispersive part is made of the Bade potential. The mixed (*ab initio*/dispersive) part is made of a linear combination of the *ab initio* and dispersive parts.

Each four-body geometry falls into one of these three categories based on its average side length \tilde{r} . Define a “lower” distance \tilde{r}_L and an “upper” distance \tilde{r}_U , where $\tilde{r}_L < \tilde{r}_U$. The part of the PES that a sample falls into is described by

$$\text{part of PES} = \begin{cases} \text{ab initio} & \text{if } \tilde{r} \leq \tilde{r}_L, \\ \text{mixed } (\text{ab initio}/\text{dispersive}) & \text{if } \tilde{r}_L < \tilde{r} < \tilde{r}_U, \\ \text{dispersive} & \text{if } \tilde{r} \geq \tilde{r}_U \end{cases} \quad (7)$$

In the mixed (*ab initio*/dispersive) part, the energy of a sample is a linear combination of the *ab initio* and dispersive parts. The fraction of the output that comes from the dispersive part is given by

$$\omega(\tilde{r}; \tilde{r}_L, \tilde{r}_U) = \begin{cases} 0 & \text{if } \tilde{r} \leq \tilde{r}_L, \\ \frac{1}{2}[1 - \cos(\pi k)] & \text{if } \tilde{r}_L < \tilde{r} < \tilde{r}_U, \\ 1 & \text{if } \tilde{r} \geq \tilde{r}_U \end{cases} \quad (8)$$

where $k = (\tilde{r} - \tilde{r}_L)/(\tilde{r}_U - \tilde{r}_L)$. In the current PES, $\tilde{r}_L = 4$ Å and $\tilde{r}_U = 4.5$ Å.

The decision to make the transition between the *ab initio* and dispersive parts depend on the average side length, and the choice of \tilde{r}_L and \tilde{r}_U , were based on observations of the *hcp* lattice geometries. By looking at the energies of geometries in the *hcp* lattice as a function of the lattice constant, it appeared that when their average side length was around 4 Å, the energy was sufficiently converged to the Bade potential.

Transition within the *ab initio* part

The *ab initio* part is further split into a part where the energies are determined directly by the MLP (the “mid-range part”), by the exponential decay extrapolation (the “short-range part”), and by a linear combination of the two (the “mixed (short/mid)-range part”).

The exponential decay fit is described earlier in the supplementary material. With no mixed (short/mid)-range part to transition between the two, there is a small discontinuity between the mid-range and the short-range parts. Depending on how small we make the “scaling step size” (ΔR) for the exponential decay fit, we can make the discontinuity very small. For example, setting $\Delta R = 0.01 \text{ \AA}$ introduces a discontinuity at the short-range/mid-range transition on the order of 0.1% for geometries with large energies (such as the tetrahedron, and other “compact” geometries), and on the order of 1 – 3% for geometries with much smaller energies (on the order of 1 cm^{-1}). For situations where only the energies are needed, this discontinuity is likely unimportant. For situations where the PES must be continuously differentiable, we can remove this discontinuity by using the same transition function and strategy we used for the transition between the *ab initio* and dispersive regions.

A four-body geometry with an average side length less than \tilde{r}_U falls into either the short-range, mid-range, or mixed (short/mid)-range parts, based on its shortest side length \tilde{R} . Define two distances \tilde{R}_L and \tilde{R}_U , where $\tilde{R}_L < \tilde{R}_U$. The part of the *ab initio* part that a sample falls into is described by

$$\text{part of the } ab \text{ initio PES} = \begin{cases} \text{short} & \text{if } \tilde{R} \leq \tilde{R}_L, \\ \text{mixed (short/mid)} & \text{if } \tilde{R}_L < \tilde{R} < \tilde{R}_U, \\ \text{mid} & \text{if } \tilde{R} \geq \tilde{R}_U \end{cases} \quad (9)$$

In the mixed (short/mid)-range part, the energy of a sample is a linear combination of the short-range and mid-range parts. The fraction of the output that comes from the mid-range part is given by

$$\omega(\tilde{R}; \tilde{R}_L, \tilde{R}_U) = \begin{cases} 0 & \text{if } \tilde{R} \leq \tilde{R}_L, \\ \frac{1}{2}[1 - \cos(\pi k)] & \text{if } \tilde{R}_L < \tilde{R} < \tilde{R}_U, \\ 1 & \text{if } \tilde{R} \geq \tilde{R}_U \end{cases} \quad (10)$$

where $k = (\tilde{R} - \tilde{R}_L)/(\tilde{R}_U - \tilde{R}_L)$. In the current PES, $\tilde{R}_L = 2.2 \text{ \AA}$ and $\tilde{r}_U = 2.25 \text{ \AA}$.

The energies from the short-range and mid-range parts of the PES are already very close to one another in the mixed (short/mid)-range region, and so the transition is fairly clean.

Limitations

Certain kinds of samples are not treated well with this mixing of, and transition between, *ab initio* and dispersive energies. For example, consider a geometry where molecules 1 and 2 are less than 2.2 \AA apart, molecules 3 and 4 are far away from them (molecules 3 and 4 may be close to one another as well). If the average side length is between \tilde{r}_L and \tilde{r}_U , the PES calculates a physically unrealistic mix of a short-range exponential wall and a long-range dispersive decay. If the average side length is greater than \tilde{r}_U , the PES categorizes this sample to be entirely dispersive. No samples in the training data exist for such geometries, and the energy produced by the PES for both cases is physically unrealistic. However, based on extrapolations of certain geometries in the *hcp* lattice training data, the four-body energies of such extreme samples are very small (typically on the order of 10^{-3} cm^{-1} to 1 cm^{-1}), and the *ab initio* total two-body energy is very large (typically on the order of 10^3 cm^{-1} to 10^5 cm^{-1}). Moreover, although physically unrealistic, the transition is still continuously differentiable.

The short-range exponential decay fit is based on the observation that, for small geometries, the energy of a four-body geometry varies exponentially as all its side lengths are scaled by the same factor. The exponential coefficient for the fit is determined by *ab initio* data that only goes down to side lengths of 2.25 \AA . The short-range energy predictions made by this PES for four-body geometries with side lengths much less than 2.2 \AA are unlikely to be accurate. In cases where the Boltzmann weight of such small four-body geometries is non-negligible, such as in solids at very high densities, such a limitation might become significant.

VIII. CONTRIBUTIONS TO THE HCP LATTICE FOR EACH GEOMETRY

We supplement the training data using samples that are based specifically on the geometries of the *hcp* lattice. The procedure for generating the samples is as follows. First, we select a reference molecule in the *hcp* lattice. Then we

consider all four-body geometries involving this reference molecule such that (1) they have at least one side length equal to the lattice constant, and (2) they have no side length more than twice the lattice constant. We find that 83 different four-body geometries satisfy these conditions. Information about all 83 geometries is provided in Table I.

TABLE I: Information about particular four-body geometries in the hcp lattice, their combinatorial frequency, and their contributions to the average four-body interaction potential energy per particle. The six side lengths in each geometry are expressed in the permutation with the lowest lexicographic order. The geometries are then ordered among themselves using their average side length, with the lexicographic order between their side lengths used as a tie-breaker. The first column is an ID number assigned to the geometry, for identification. The second column contains N_c , the number of times that geometry appears under the aforementioned conditions for which they were selected. Columns 3 to 8 are the ratio of the six side lengths to the lattice constant. Column 9 is the total contribution of the geometry to the average four-body interaction potential energy per particle (units of cm^{-1}), when the lattice constant is 2.2 Å.

| ID | N_c | r_{12} | r_{13} | r_{14} | r_{23} | r_{24} | r_{34} | $V_4^{(\text{tot})}$ |
|----|-------|----------|------------|---------------|---------------|---------------|---------------|----------------------|
| 0 | 8 | 1 | 1 | 1 | 1 | 1 | 1 | 398.3489 |
| 1 | 48 | 1 | 1 | 1 | 1 | 1 | $\sqrt{2}$ | 1767.6561 |
| 2 | 12 | 1 | 1 | 1 | 1 | 1 | $\sqrt{8/3}$ | 510.3478 |
| 3 | 36 | 1 | 1 | 1 | 1 | 1 | $\sqrt{3}$ | 1673.2181 |
| 4 | 12 | 1 | 1 | $\sqrt{2}$ | $\sqrt{2}$ | 1 | 1 | 777.0374 |
| 5 | 144 | 1 | 1 | 1 | 1 | $\sqrt{2}$ | $\sqrt{3}$ | 938.2455 |
| 6 | 48 | 1 | 1 | 1 | 1 | $\sqrt{2}$ | $\sqrt{11/3}$ | 333.7082 |
| 7 | 24 | 1 | 1 | 1 | $\sqrt{2}$ | $\sqrt{2}$ | $\sqrt{8/3}$ | 26.8497 |
| 8 | 72 | 1 | 1 | 1 | 1 | $\sqrt{3}$ | $\sqrt{3}$ | -72.8998 |
| 9 | 48 | 1 | 1 | 1 | 1 | $\sqrt{8/3}$ | $\sqrt{11/3}$ | -34.8335 |
| 10 | 48 | 1 | 1 | 1 | 1 | $\sqrt{3}$ | $\sqrt{11/3}$ | -112.8734 |
| 11 | 96 | 1 | 1 | 1 | 1 | $\sqrt{3}$ | 2 | -263.0247 |
| 12 | 24 | 1 | 1 | $\sqrt{2}$ | $\sqrt{2}$ | 1 | $\sqrt{11/3}$ | 23.2044 |
| 13 | 24 | 1 | 1 | 1 | $\sqrt{2}$ | $\sqrt{2}$ | 2 | 31.7028 |
| 14 | 24 | 1 | 1 | 1 | 1 | $\sqrt{11/3}$ | $\sqrt{11/3}$ | -107.4177 |
| 15 | 48 | 1 | 1 | 1 | $\sqrt{2}$ | $\sqrt{3}$ | $\sqrt{3}$ | 3.9874 |
| 16 | 144 | 1 | 1 | $\sqrt{2}$ | $\sqrt{3}$ | 1 | $\sqrt{3}$ | 589.1818 |
| 17 | 48 | 1 | 1 | $\sqrt{2}$ | $\sqrt{8/3}$ | 1 | $\sqrt{11/3}$ | 47.4894 |
| 18 | 48 | 1 | 1 | 1 | $\sqrt{2}$ | $\sqrt{3}$ | $\sqrt{11/3}$ | -0.1676 |
| 19 | 48 | 1 | 1 | $\sqrt{2}$ | 1 | $\sqrt{3}$ | $\sqrt{11/3}$ | 17.5318 |
| 20 | 24 | 1 | 1 | 1 | $\sqrt{8/3}$ | $\sqrt{3}$ | $\sqrt{3}$ | 8.1791 |
| 21 | 12 | 1 | 1 | $\sqrt{3}$ | $\sqrt{8/3}$ | $\sqrt{2}$ | $\sqrt{2}$ | 49.4868 |
| 22 | 8 | 1 | 1 | 1 | $\sqrt{3}$ | $\sqrt{3}$ | $\sqrt{3}$ | 3.3276 |
| 23 | 24 | 1 | 1 | $\sqrt{3}$ | 1 | $\sqrt{3}$ | $\sqrt{3}$ | 2.5747 |
| 24 | 24 | 1 | 1 | $\sqrt{2}$ | 1 | $\sqrt{11/3}$ | $\sqrt{11/3}$ | 1.9198 |
| 25 | 48 | 1 | 1 | $\sqrt{2}$ | $\sqrt{11/3}$ | 1 | $\sqrt{11/3}$ | 78.6803 |
| 26 | 48 | 1 | 1 | $\sqrt{8/3}$ | $\sqrt{3}$ | 1 | $\sqrt{11/3}$ | 147.4124 |
| 27 | 48 | 1 | 1 | $\sqrt{2}$ | $\sqrt{2}$ | $\sqrt{3}$ | $\sqrt{3}$ | 5.5033 |
| 28 | 12 | 1 | $\sqrt{2}$ | $\sqrt{3}$ | $\sqrt{3}$ | $\sqrt{2}$ | 1 | 56.9016 |
| 29 | 48 | 1 | 1 | $\sqrt{11/3}$ | $\sqrt{2}$ | $\sqrt{2}$ | $\sqrt{8/3}$ | 74.2656 |
| 30 | 48 | 1 | 1 | $\sqrt{8/3}$ | 1 | $\sqrt{11/3}$ | $\sqrt{11/3}$ | 0.8395 |
| 31 | 48 | 1 | 1 | $\sqrt{3}$ | 1 | $\sqrt{3}$ | 2 | 1.9873 |
| 32 | 48 | 1 | 1 | $\sqrt{3}$ | $\sqrt{3}$ | 1 | 2 | 130.0325 |
| 33 | 96 | 1 | 1 | $\sqrt{3}$ | $\sqrt{2}$ | $\sqrt{2}$ | 2 | 19.3653 |
| 34 | 96 | 1 | 1 | $\sqrt{3}$ | $\sqrt{3}$ | $\sqrt{2}$ | $\sqrt{3}$ | 115.7225 |
| 35 | 48 | 1 | 1 | $\sqrt{2}$ | $\sqrt{3}$ | $\sqrt{3}$ | $\sqrt{11/3}$ | 2.2902 |
| 36 | 48 | 1 | 1 | $\sqrt{3}$ | $\sqrt{2}$ | $\sqrt{3}$ | $\sqrt{11/3}$ | 2.2277 |
| 37 | 48 | 1 | $\sqrt{2}$ | $\sqrt{3}$ | $\sqrt{11/3}$ | $\sqrt{3}$ | 1 | 77.3423 |
| 38 | 24 | 1 | 1 | $\sqrt{3}$ | $\sqrt{8/3}$ | $\sqrt{3}$ | $\sqrt{3}$ | 6.0805 |
| 39 | 24 | 1 | 1 | $\sqrt{2}$ | 2 | $\sqrt{3}$ | $\sqrt{3}$ | 5.6200 |
| 40 | 48 | 1 | 1 | 2 | $\sqrt{2}$ | $\sqrt{3}$ | $\sqrt{3}$ | 11.4372 |
| 41 | 48 | 1 | $\sqrt{2}$ | $\sqrt{3}$ | $\sqrt{3}$ | 2 | 1 | 19.5027 |
| 42 | 24 | 1 | $\sqrt{2}$ | $\sqrt{2}$ | $\sqrt{3}$ | $\sqrt{3}$ | $\sqrt{8/3}$ | 1.7976 |
| 43 | 48 | 1 | 1 | $\sqrt{2}$ | $\sqrt{11/3}$ | $\sqrt{3}$ | $\sqrt{11/3}$ | 4.0230 |

Table I: Continued from previous page...

| ID | N_c | r_{12} | r_{13} | r_{14} | r_{23} | r_{24} | r_{34} | $V_4^{(\text{tot})}$ |
|----|-------|----------|---------------|---------------|---------------|---------------|---------------|----------------------|
| 44 | 48 | 1 | 1 | $\sqrt{11/3}$ | $\sqrt{2}$ | $\sqrt{3}$ | $\sqrt{11/3}$ | 3.2812 |
| 45 | 48 | 1 | 1 | $\sqrt{11/3}$ | $\sqrt{3}$ | $\sqrt{2}$ | $\sqrt{11/3}$ | 31.6711 |
| 46 | 48 | 1 | $\sqrt{2}$ | $\sqrt{3}$ | $\sqrt{11/3}$ | $\sqrt{11/3}$ | 1 | 34.7712 |
| 47 | 48 | 1 | 1 | $\sqrt{11/3}$ | $\sqrt{3}$ | $\sqrt{8/3}$ | $\sqrt{3}$ | 25.8993 |
| 48 | 12 | 1 | $\sqrt{8/3}$ | $\sqrt{11/3}$ | $\sqrt{11/3}$ | $\sqrt{8/3}$ | 1 | 15.2368 |
| 49 | 24 | 1 | 1 | 2 | $\sqrt{8/3}$ | $\sqrt{3}$ | $\sqrt{3}$ | 8.0599 |
| 50 | 48 | 1 | $\sqrt{2}$ | $\sqrt{8/3}$ | $\sqrt{3}$ | $\sqrt{11/3}$ | $\sqrt{2}$ | 5.6212 |
| 51 | 24 | 1 | 1 | $\sqrt{3}$ | $\sqrt{11/3}$ | $\sqrt{3}$ | $\sqrt{3}$ | 8.5996 |
| 52 | 48 | 1 | 1 | $\sqrt{8/3}$ | $\sqrt{3}$ | $\sqrt{11/3}$ | $\sqrt{11/3}$ | 1.9287 |
| 53 | 96 | 1 | 1 | $\sqrt{3}$ | $\sqrt{3}$ | $\sqrt{3}$ | 2 | 7.0128 |
| 54 | 24 | 1 | 1 | 2 | $\sqrt{3}$ | $\sqrt{3}$ | $\sqrt{3}$ | 8.9254 |
| 55 | 48 | 1 | $\sqrt{3}$ | $\sqrt{3}$ | $\sqrt{3}$ | 2 | 1 | 24.0374 |
| 56 | 24 | 1 | $\sqrt{2}$ | $\sqrt{3}$ | $\sqrt{3}$ | $\sqrt{2}$ | $\sqrt{11/3}$ | 2.1125 |
| 57 | 48 | 1 | $\sqrt{2}$ | $\sqrt{3}$ | $\sqrt{11/3}$ | $\sqrt{2}$ | $\sqrt{3}$ | 12.3522 |
| 58 | 48 | 1 | $\sqrt{2}$ | 2 | $\sqrt{3}$ | $\sqrt{3}$ | $\sqrt{2}$ | 13.9028 |
| 59 | 48 | 1 | 1 | $\sqrt{3}$ | $\sqrt{11/3}$ | $\sqrt{3}$ | $\sqrt{11/3}$ | 7.6466 |
| 60 | 48 | 1 | 1 | $\sqrt{11/3}$ | $\sqrt{3}$ | $\sqrt{3}$ | $\sqrt{11/3}$ | 7.0239 |
| 61 | 24 | 1 | $\sqrt{3}$ | $\sqrt{3}$ | $\sqrt{11/3}$ | $\sqrt{11/3}$ | 1 | 7.5321 |
| 62 | 48 | 1 | $\sqrt{2}$ | $\sqrt{3}$ | $\sqrt{3}$ | $\sqrt{3}$ | $\sqrt{3}$ | 2.3053 |
| 63 | 24 | 1 | $\sqrt{3}$ | $\sqrt{3}$ | $\sqrt{3}$ | $\sqrt{3}$ | $\sqrt{2}$ | 2.4616 |
| 64 | 48 | 1 | $\sqrt{8/3}$ | $\sqrt{11/3}$ | $\sqrt{11/3}$ | $\sqrt{11/3}$ | 1 | 20.9388 |
| 65 | 24 | 1 | $\sqrt{3}$ | $\sqrt{11/3}$ | 2 | $\sqrt{3}$ | 1 | 16.0475 |
| 66 | 48 | 1 | $\sqrt{2}$ | $\sqrt{11/3}$ | $\sqrt{3}$ | $\sqrt{8/3}$ | $\sqrt{3}$ | 4.6222 |
| 67 | 24 | 1 | 1 | $\sqrt{8/3}$ | 2 | $\sqrt{11/3}$ | $\sqrt{11/3}$ | 1.9854 |
| 68 | 12 | 1 | $\sqrt{3}$ | 2 | 2 | $\sqrt{3}$ | 1 | 8.9282 |
| 69 | 48 | 1 | $\sqrt{2}$ | 2 | $\sqrt{11/3}$ | $\sqrt{3}$ | $\sqrt{2}$ | 16.0005 |
| 70 | 48 | 1 | 1 | $\sqrt{11/3}$ | $\sqrt{3}$ | $\sqrt{11/3}$ | $\sqrt{11/3}$ | 2.8300 |
| 71 | 48 | 1 | $\sqrt{3}$ | $\sqrt{3}$ | $\sqrt{3}$ | $\sqrt{11/3}$ | $\sqrt{2}$ | 4.0850 |
| 72 | 12 | 1 | $\sqrt{3}$ | $\sqrt{3}$ | $\sqrt{3}$ | $\sqrt{3}$ | $\sqrt{8/3}$ | 0.3714 |
| 73 | 48 | 1 | 1 | $\sqrt{3}$ | $\sqrt{11/3}$ | $\sqrt{11/3}$ | 2 | 2.6144 |
| 74 | 24 | 1 | $\sqrt{2}$ | $\sqrt{2}$ | $\sqrt{11/3}$ | $\sqrt{11/3}$ | 2 | 0.0388 |
| 75 | 48 | 1 | $\sqrt{2}$ | $\sqrt{3}$ | $\sqrt{11/3}$ | $\sqrt{3}$ | $\sqrt{11/3}$ | 1.0870 |
| 76 | 48 | 1 | $\sqrt{2}$ | $\sqrt{3}$ | $\sqrt{11/3}$ | $\sqrt{11/3}$ | $\sqrt{3}$ | 1.1112 |
| 77 | 24 | 1 | 1 | $\sqrt{3}$ | 2 | 2 | 2 | 1.2307 |
| 78 | 48 | 1 | $\sqrt{8/3}$ | $\sqrt{3}$ | $\sqrt{11/3}$ | $\sqrt{3}$ | $\sqrt{3}$ | 1.0489 |
| 79 | 48 | 1 | $\sqrt{3}$ | $\sqrt{11/3}$ | 2 | $\sqrt{3}$ | $\sqrt{3}$ | 0.8478 |
| 80 | 24 | 1 | $\sqrt{11/3}$ | $\sqrt{11/3}$ | $\sqrt{11/3}$ | $\sqrt{11/3}$ | $\sqrt{3}$ | 0.0701 |
| 81 | 24 | 1 | $\sqrt{3}$ | $\sqrt{3}$ | 2 | 2 | 2 | -0.0329 |
| 82 | 96 | 1 | $\sqrt{3}$ | $\sqrt{11/3}$ | 2 | $\sqrt{11/3}$ | $\sqrt{11/3}$ | 0.0262 |